https://doi.org/10.5194/egusphere-2026-5859
Preprint. Discussion started: 4 November 2026
© Author(s) 2026. CC BY 4.0 License.

ORCHIDEE-Hg v1.0 (rev. 9721): A new global land-surface model for mercury dynamics – Part 1: Model description and evaluation in temperate regions

Laura Sereni[1,*], Elodie Salmon[2], Simon Bowring[2], Bertrand Guenet[3], Erfan Jahangir[1], Ronny Lauerwald[4], Dingwu Liu[4], Haicheng Zhang[5], Hélène Angot[1,*]

1. Univ. Grenoble Alpes, CNRS, INRAE, IRD, Grenoble INP, IGE, Grenoble, France.
2. Laboratoire des Sciences du Climat et de l'Environnement (LSCE), IPSL-CEA-CNRS-UVSQ, Université Paris-Saclay, Gif-sur-Yvette, France
3. Laboratoire de Geologie ENS, PSL Research University, CNRS, UMR 8538, IPSL, Paris, France
4. Université Paris-Saclay, INRAe/AgroParisTech, UMR EcoSys, Palaiseau, France
5. Carbon-Water Research Station in Karst Regions of Northern Guangdong, School of Geography and Planning, Sun Yat-Sen University, Guangzhou, 510006, China

*Corresponding authors: laura.sereni@univ-grenoble-alpes.fr ; laurasereni@yahoo.fr; helene.angot@univ-grenoble-alpes.fr

Short summary

Mercury (Hg) is a toxic global pollutant whose terrestrial cycling is strongly influenced by vegetation, soils, and environmental changes. We present ORCHIDEE-Hg v1.0, a global mechanistic model of the terrestrial Hg cycle simulating atmospheric Hg deposition inputs, vegetation uptake, soil storage, dissolved Hg dynamics, and soil re-emissions. Evaluation against observations shows that the model successfully reproduces Hg concentrations, stocks, and fluxes across key terrestrial compartments.

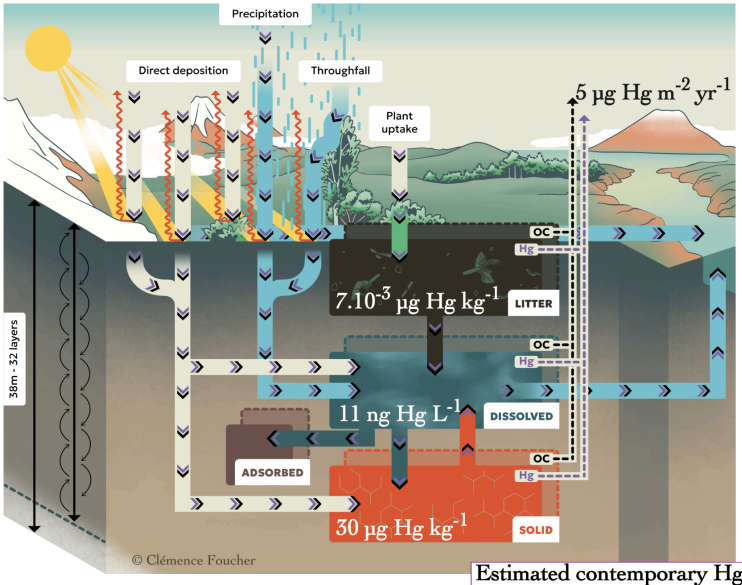
https://doi.org/10.5194/egusphere-2026-5859
Preprint. Discussion started: 4 November 2026
© Author(s) 2026. CC BY 4.0 License.

Abstract

Mercury (Hg) is a highly toxic global pollutant that is transported throughout the atmosphere and transferred to terrestrial ecosystems through vegetation uptake and atmospheric wet and dry deposition. Owing to its strong association with organic carbon (OC) and long residence time, soils represent the largest Hg reservoirs. Environmental changes can, however, alter Hg stocks and fluxes, potentially enhancing Hg emissions to the atmosphere or export to riverine systems. Existing global models have yet to fully capture the dynamics of dissolved Hg and its transport through terrestrial hydrological pathways, as well as Hg storage and remobilization in deep soil layers, limiting their ability to represent terrestrial Hg responses to environmental change.

Here, we present the first version of ORCHIDEE-Hg (ORCHIDEE-Hg v1.0), a global land-surface model of the terrestrial Hg cycle developed within the well-established ORCHIDEE framework. The model uniquely integrates explicit representations of dissolved carbon species and vertical discretization of soil across 15 plant functional types. ORCHIDEE-Hg represents the terrestrial Hg cycle, from atmospheric wet and dry deposition and vegetation uptake to soil storage, dissolved Hg dynamics, and atmospheric re-emissions. We evaluate ORCHIDEE-Hg against recent observations of vegetation Hg concentrations, litterfall Hg fluxes, and soil stocks across two temperate regions. The model successfully reproduces observed median Hg concentrations, stocks, and fluxes within and between key compartments. This evaluation provides a robust foundation for investigating the controls of terrestrial Hg cycling. A companion study will assess model sensitivity to key parameters and processes, providing a detailed understanding of model behavior before using ORCHIDEE-Hg to investigate changes in soil Hg stocks and fluxes under environmental perturbations, including climate change, land-use and land-cover change, and changes in atmospheric deposition.

https://doi.org/10.5194/egusphere-2026-5859
Preprint. Discussion started: 4 November 2026
© Author(s) 2026. CC BY 4.0 License.



Estimated contemporary Hg concentrations (0-20 cm) and fluxes per compartment

https://doi.org/10.5194/egusphere-2026-5859
Preprint. Discussion started: 4 November 2026
© Author(s) 2026. CC BY 4.0 License.

Introduction

Mercury (Hg) is a potent neurotoxin and a global pollutant of major concern due to its adverse health effects (Driscoll et al., 2013), long-range atmospheric transport, and cycling among the atmosphere, terrestrial ecosystems, and oceans (Obrist et al., 2018). Both geogenic sources (e.g., volcanic activity, rock weathering) and anthropogenic activities (e.g., chlor-alkali production, artisanal gold mining, coal-fired power plants) contribute to Hg emissions and releases to the atmosphere and terrestrial/aquatic systems. In response to the health risks posed by Hg, international environmental policies such as the Minamata Convention aim to reduce anthropogenic emissions, which were estimated at approximately 2.5 $Gg \cdot yr^{-1}$ in 2015 (Sonke et al., 2023). However, several other environmental factors, including climate change (AMAP, 2021; Sonke et al., 2023), land-use and land-cover change (Feinberg et al., 2024; Zhang et al., 2016), and changes in atmospheric chemical composition (Feinberg et al., 2026), may modulate the effectiveness of direct emission reduction (Dastoor et al., 2025). Besides, due to its very long residence time in soils and oceans (10^2–10^3 years), compared with its approximately 1-year atmospheric residence time (Amos et al., 2013; Selin et al., 2008), Hg progressively accumulates in these compartments. As a result, these large legacy pools continuously re-emit Hg to the atmosphere, meaning that reductions in current anthropogenic emissions are only gradually reflected in atmospheric Hg concentrations.

Terrestrial ecosystems play a pivotal role in the global Hg cycle, acting both as major reservoirs, storing approximately 235−1150 Gg of Hg in the upper 20 cm of soil (Amos et al., 2015, 2013; Lim et al., 2020; Selin et al., 2008), and as dynamic interfaces that engage in active bidirectional exchanges with the atmosphere (Sommar et al., 2020; Zhu et al., 2016) and export Hg to riverine systems (Fabre et al., 2024; Panagos et al., 2021). Vegetation, a key component of terrestrial ecosystems, actively takes up atmospheric Hg and, to a lesser extent, soil Hg, while also contributing to soil organic carbon (OC) through litterfall and root turnover, thereby promoting Hg retention (Wang et al., 2019; Zhou et al., 2021). Plant Hg uptake, which is related to foliar photosynthetic activity, contributes to seasonal variations in surface atmospheric Hg concentrations (Fu et al., 2019; Jiskra et al., 2018) and is also strongly influenced by environmental factors such as climate (Jia et al., 2026).

https://doi.org/10.5194/egusphere-2026-5859
Preprint. Discussion started: 4 November 2026
© Author(s) 2026. CC BY 4.0 License.

Climate change may threaten Hg stocks and fluxes in terrestrial ecosystems by altering vegetation dynamics (Feinberg et al., 2024) and soil OC dynamics (Chen et al., 2024a). In addition, changes in soil temperature and moisture may trigger the remobilization of stored Hg (Hararuk et al., 2013), particularly in permafrost regions, where an estimate of 600 Gg of Hg are stored in deep frozen soil layers (Lim et al., 2020).

Despite the recognized importance of the terrestrial biosphere in the global Hg cycle, global mechanistic models of terrestrial Hg dynamics remain underdeveloped compared with atmospheric and oceanic models (Dastoor et al., 2025). Recent developments have focused primarily on statistical estimates of Hg soils stocks (Guo et al., 2024; Liu et al., 2023) or on relatively fast-turnover reservoirs such as vegetation and litter (Yuan et al., 2023). To date, three mechanistic models of the terrestrial Hg cycle have been developed by exploiting the strong association between soil Hg and OC. These models build on land-surface models that represent vegetation, soil, and litter OC cycling and incorporate Hg dynamics into these frameworks. The Global Terrestrial Mercury Model (GTMM) provided the first estimates of Hg remobilization under climate change, predicting an approximately threefold increase in soil Hg emissions relative to the pre-industrial state (Smith-Downey et al., 2010). However, the GTMM represents only the upper 30 cm of soil and does not account for Hg in soil solution (i.e., the dissolved Hg pool in soil porewater) or its export through runoff. More recently, Schaefer et al., (2020) focused on Hg remobilization in permafrost regions and provided the first estimate of Hg release associated with permafrost thaw in the Yukon basin. However, the lack of an explicit representation of Hg in soil solution, as well as the limited representation of spatial variability in permafrost Hg concentrations, may limit the accuracy of their estimates of riverine Hg exports. Moreover, both models lack robust, independent evaluations of their simulated Hg stocks and fluxes, thereby limiting confidence in their projections. Finally, CLM5-Hg (Yuan et al., 2023) was developed to represent the continental Hg cycle, including the soil compartment, but its results have focused primarily on more labile pools, such as litter and vegetation, limiting its assessment of Hg dynamics in longer-lived terrestrial reservoirs. Despite recent advances, existing terrestrial Hg models therefore do not explicitly represent several processes that are critical for understanding the fate and mobility of Hg under environmental change, particularly the dynamics of dissolved Hg and its transport through terrestrial hydrological pathways, as well as Hg storage and remobilization in deep soil layers. These limitations hinder the ability

https://doi.org/10.5194/egusphere-2026-5859
Preprint. Discussion started: 4 November 2026
© Author(s) 2026. CC BY 4.0 License.

of current models to simultaneously represent Hg retention in terrestrial ecosystems, atmospheric re-emission, and riverine export, and to assess their responses to global change.

To address these limitations, we developed ORCHIDE-Hg, a new mechanistic model of the terrestrial Hg cycle. ORCHIDEE-Hg v1.0 includes deposition to vegetation and soils surfaces and associated re-emission as well as a representation of Hg uptake by vegetation. The model explicitly distinguishes dissolved and solid-phase soil Hg pools, and vertically discretizes the soil profile down to 38 m. The model is built on ORCHIDEE-MICT-PEAT-LEAK (Bowring et al., 2019, 2020; Qiu et al., 2019), a recent version of the established land-surface model ORCHIDEE with a robust and extensively validated representation of vegetation, soil, and OC dynamics as well as some high latitude features (Guimberteau et al., 2018), with peatland related process (Qiu et al., 2019) and with lateral OC transport (Lauerwald et al., 2017; Zhang et al., 2022). This framework enables Hg dynamics to be mechanistically coupled to the environmental processes that regulate its terrestrial storage, mobility, and fluxes, providing a basis for assessing Hg responses to climate change, land-use and land-cover change, and changes in atmospheric Hg deposition.

Although this mechanistic Hg model is ultimately designed to investigate the impacts of global change on the terrestrial Hg cycle, the present study focuses on describing the first version of the model (ORCHIDEE-Hg v1.0) and evaluating its simulations against observational data from temperate regions. Evaluation of Hg dynamics in high-latitude ecosystems, including peatland and permafrost regions will be addressed in future model developments. Model sensitivity to key parameters will be assessed in detail in a companion study, providing a systematic evaluation of model behavior before ORCHIDEE-Hg is used to investigate the response of the terrestrial Hg cycle to environmental change.

2. Material and methods

2.1. Model description

2.1.1 Model overview

ORCHIDEE-Hg was developed from the land surface model ORCHIDEE (Organising Carbon and Hydrology In Dynamic Ecosystems (Krinner et al., 2005)), a well-established framework for simulating ecosystem OC dynamics. ORCHIDEE explicitly represents 15 plant functional

https://doi.org/10.5194/egusphere-2026-5859
Preprint. Discussion started: 4 November 2026
© Author(s) 2026. CC BY 4.0 License.

types (PFTs), litter, soil solid (SOC) and dissolved (DOC) OC pools, as well as inland waters (e.g., rivers, lakes, and wetlands). Leveraging the strong affinity between Hg and OC (Ballabio et al., 2021; Obrist et al., 2011; Skyllberg et al., 2000), we implemented a mechanistic terrestrial Hg cycle in this framework.

ORCHIDEE-Hg is derived from three specialized versions of ORCHIDEE: ORCHIDEE-MICT-LEAK (revision 5459 (Bowring et al., 2019, 2020)), which includes an explicit representation of dissolved carbon transport and cycling through the soil column and river networks as well as permafrost specific processes, ORCHIDEE-Clateral, which represents in addition erosion, transport, and deposition of sediments and associated translocation of particulate organic carbon from hillslopes along the river networks to the coast or depositional zones in floodplains (Zhang et al., 2022); and ORCHIDEE-PEAT (revision 4596 (Qiu et al., 2019)), which adds specialized PFTs, hydrological properties, and processes of preservation and decomposition of OC that are characteristic of northern peatlands. While the current presentation of ORCHIDEE-Hg v1.0 focuses on temperate regions and does not explicitly include Hg processes over permafrost areas or peatlands, we use this framework to support future development for high latitude regions which are of particular interest due to their substantial Hg stocks (Lim et al., 2020; Schuster et al., 2018) and the numerous interacting processes that influence Hg dynamics in these environments (Bring et al., 2016; Schuur and Mack, 2018).

As described in Fig. 1 and further detailed below, ORCHIDEE-Hg v1.0 (rev. 9721) accounts for Hg assimilation by vegetation and deposition to soils via litterfall and throughfall, and direct wet and dry deposition, as well as storage in litter and soils, re-emissions of gaseous elemental Hg (Hg^0) to the atmosphere, and vertical transport and lateral export through soil solution.

2.1.2 Hg deposition and uptake pathways

Atmospheric Hg is predominantly present as relatively stable Hg^0, which can persist for several months to about a year and thus undergo long-range atmospheric transport. Hg^0 can be oxidized to reactive divalent Hg (Hg^{2+}), primarily through reactions involving bromine radicals and other atmospheric oxidants (Shah et al., 2021); Hg^{2+} is more water-soluble and has a strong affinity for aerosols and atmospheric surfaces, favouring its removal through wet and dry deposition (Selin, 2009).

https://doi.org/10.5194/egusphere-2026-5859
Preprint. Discussion started: 4 November 2026
© Author(s) 2026. CC BY 4.0 License.

In ORCHIDEE-Hg v1.0, atmospheric Hg inputs to terrestrial surfaces occur in the form of wet deposition of Hg^{2+}, and dry deposition of Hg^0 and Hg^{2+}. Dry-deposited Hg^0 and Hg^{2+} can be either assimilated by vegetation, or remain on leaf or soil surfaces (Fig. 1). Studies have shown that Hg^0 does not significantly contribute to the total Hg found in background soils (Friedli et al., 2007; Skyllberg et al., 2000). Therefore, all non-assimilated Hg^0 is assumed to be revolatilized, while Hg^{2+} remains on leaf surfaces and is washed off by rainfall (i.e. throughfall fluxes).

Following Smith-Downey et al., (2010), we assume that the fraction of Hg from dry deposition permanently fixed by leaves is equal to the product of f_{fixed} and the total Hg^0 and Hg^{2+} dry deposition, with f_{fixed} calculated following (1):

$$f_{fixed} = 0.25 \frac{LAI}{1.25} \; for \; LAI \leq 1.25; \; 0.25 \; for \; LAI > 1.25 \qquad (1)$$

Hg^{2+} that is not assimilated is subject to photoreduction with $f_{photoreduction}$ representing the fraction of Hg^{2+} deposited to soil and leaves surfaces subject to photoreduction, following (2):

$$f_{photoreduction} = 0.67 \times exp(-0.016\, s) \quad (2)$$

where s is the short-wave solar radiation flux (W m^{-2}) (Smith-Downey et al., 2010).

Hg^{2+} in dry phase, not assimilated by leaves nor photoreduced, resides in the surface leaf pool and is washed off during precipitation events (i.e., throughfall flux) (Fig. 1).

Hg^{2+} in wet phase deposits to soil surfaces or to the vegetation canopy and is subject to the same photoreduction process as Hg^{2+} in dry phase (parameterized with $f_{photoreduction}$). The non-photoreduced fraction of wet Hg^{2+} is assumed to deposit to soils and leach into the dissolved pool (Fig.1).

Hg originating from bedrock weathering that represents a minor part of Hg in soils (Gao et al., 2023) was not accounted for.

https://doi.org/10.5194/egusphere-2026-5859
Preprint. Discussion started: 4 November 2026
© Author(s) 2026. CC BY 4.0 License.

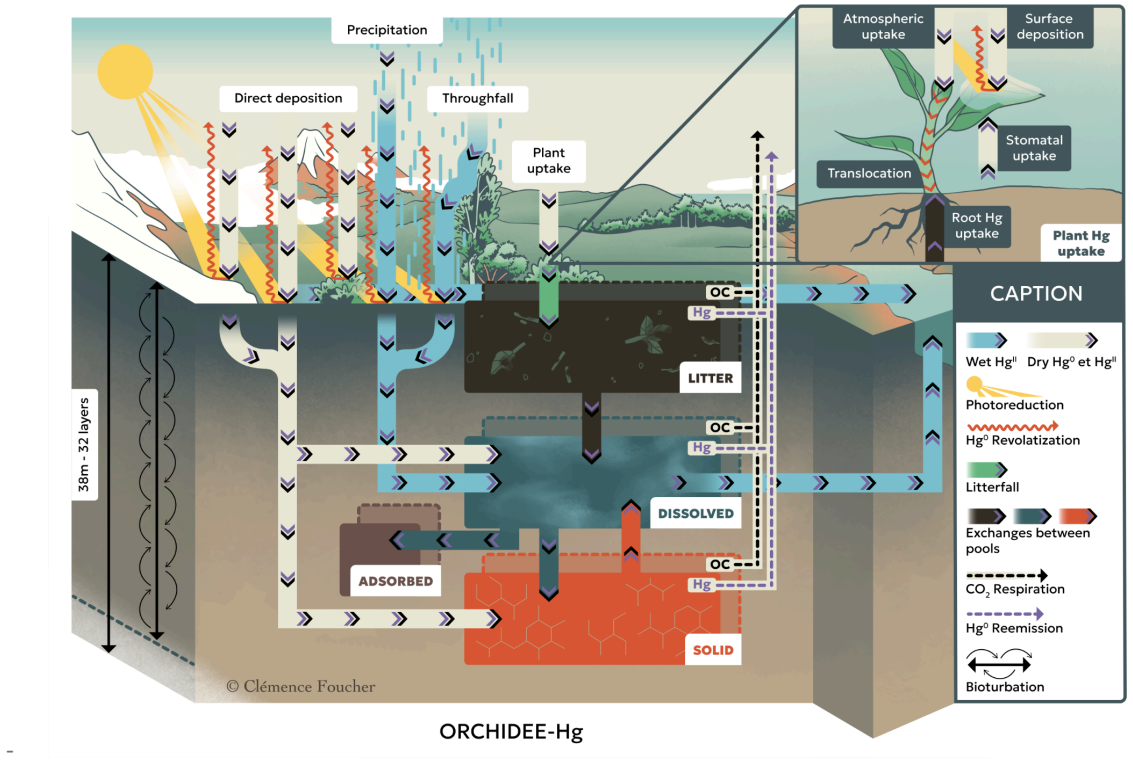


Figure 1: Schematic view of the main Hg processes represented in ORCHIDEE-Hg v1.0. Direct deposition refers to non vegetation-mediated deposition, i.e., to bare soils or water/snow.

2.1.3 Hg in vegetation

While foliar uptake of dry Hg^0 and Hg^{2+} dominates Hg absorption by vegetation, recent meta-analyses indicate that approximately 15% of soil Hg deposition originates from non-foliar tissues, including root absorption and Hg translocation within plant compartments (Zhou and Obrist, 2021). However, the environmental controls on Hg uptake and translocation in non-foliar tissues remain poorly understood, and only foliar uptake of dry Hg is currently mechanistically parameterized (see section 2.1.2., Eq (1)).

To account for Hg distribution across plant compartments beyond the leaves, we relied on the dataset published by Zhou and Obrist (2021) to derive plant compartments allocation coefficients (k_{alloc}). These coefficients link Hg concentrations in leaves to those in other plant tissues for each PFT. To address data limitations, we grouped the eight model plant

https://doi.org/10.5194/egusphere-2026-5859
Preprint. Discussion started: 4 November 2026
© Author(s) 2026. CC BY 4.0 License.

compartments (leaves, fruits, reserve carbon, aboveground sapwood, aboveground heartwood, belowground sapwood, belowground heartwood, and roots) into three broader categories based on similarities in carbon residence times and decomposition rates (see Section 2.1.4 for rationale). We then defined two allocation coefficients: k_{alloc_ba} for ligneous aboveground tissues (aboveground sapwood and heartwood) and k_{alloc_bb} for ligneous belowground tissues (roots, belowground sapwood, and heartwood). Each coefficient was calculated as the ratio of mean Hg concentration in branches (for k_{alloc_ba}) or roots (for k_{alloc_bb}) to the mean Hg concentration in leaves from the Zhou and Obrist (2021) database, see Table A1. These coefficients were then used to estimate Hg concentrations in non-foliar tissues based on the Hg assimilated by leaves.

2.1.4 Litter and soil Hg cycling

The Hg cycle is simulated within the OC cycling framework, which is fully described in Bowring et al., (2019). In this framework, each of the eight plant tissues (leaves, fruits, carbon reserves, aboveground sapwood, belowground sapwood, aboveground heartwood, belowground heartwood, and roots) is characterized by lignin content and turnover time, which govern their degradability once they enter the litter pool. Litter is divided into two aboveground and two belowground pools, each further split into structural and metabolic fractions. OC degradation in litter is controlled by soil temperature, moisture, and lignin content (for structural pools). SOC consists of three pools: active, slow, and passive while DOC consists of seven similar pools like those in litter and SOC. A fraction of each DOC pool is adsorbed to mineral soil, where it does not participate in OC degradation or respiration until desorption (see Section 2.1.5). Litter degradation produces carbon dioxide (CO_2), SOC and DOC, with belowground plant decomposition directly contributing to depth-specific SOC and DOC pools in the upper 2 meters of soil. The three SOC pools are derived from DOC pools and can revert to DOC and CO_2 through microbial degradation. C inputs from the decomposition and transformation of litter, SOC and DOC, as well as their vertical transport through bio- or cryoturbation are resolved across the full 38-meter soil profile, while DOC sorption, and vertical and lateral transport with water fluxes are limited to the top 2 meters (see Section 2.1.5). Litter, soil and dissolved pools decomposition in each layer are defined

https://doi.org/10.5194/egusphere-2026-5859
Preprint. Discussion started: 4 November 2026
© Author(s) 2026. CC BY 4.0 License.

by different decomposition rates modulated by soil temperature and soil moisture **(Bowring et al., 2019)**, and by clay content for soil and dissolved pools.

We associate a Hg pool to each OC pool: litter (Litt-Hg), dissolved (dHg), and soil (soil-Hg) pools at each soil depth. As OC degrades through heterotrophic respiration or transformation into other OC pools (e.g., litter → DOC, DOC → SOC, or SOC → DOC), the associated Hg is mobilized under the same environmental controls as OC. A fraction of the mobilized Hg is transferred to the subsequent OC pool, while another fraction is reduced and emitted to the atmosphere as Hg^0. Hg^0 emissions to the atmosphere are proportional to the amount of respired OC, but scaled by a reduction factor (fd_{Hg} (Smith-Downey et al., 2010)). Similarly, the fraction of Hg transferred to other pools is proportional to the amount of OC transformed, scaled by (1 – fd_{Hg}), meaning higher fd_{Hg} values result in slower Hg transfer between pools.

The GTMM model (Smith-Downey et al., 2010) initially set fd_{Hg} to 0.16, based on Hg/C ratios (0.3 μg g^{-1}) calculated for the O horizons in the United States soil samples (Smith et al., 2005). Using European soil survey data, in which Hg and OC values were measured in more than 20,000 samples from the 0–20 cm soil layer (Ballabio et al., 2021; Orgiazzi et al., 2018), we derived a mean Hg/C ratio of 0.98 μg g^{-1} after excluding values falling outside +/- 1.5 times the interquartile range (IQR) (Chambers, 1998; Mcgill et al., 1978). This ratio is three times larger than the Hg/C ratio reported by Smith et al., (2005). We therefore adjusted fd_{Hg} to 33% of its initial value of 0.16, resulting in fd_{Hg}= 0.053.

2.1.5 Special features for dissolved substances (DOC and dHg)

The model includes the explicit representation of dissolved substances in soil solution and the vertical discretization of soil and water columns, which incorporate processes such as (1) sorption to minerals, (2) vertical transport by water fluxes through advection or diffusion, (3) and horizontal export to rivers. These processes are extensively described in Camino-Serrano et al., (2018) and can be summarized as follows:

Sorption and desorption of DOC and dHg are defined based on adsorption coefficients (Kd_{DOC} and Kd_{dHg} respectively). Kd_{DOC} depends on soil clay content following (3), while Kd_{dHg} is set as $10^{-5.3}$ (Allison et al., 2010).

$$Kd_{DOC} = 10^{(-3.1+0.2 \times log\,(clay) + log\,(l/2))} \quad (3)$$

https://doi.org/10.5194/egusphere-2026-5859
Preprint. Discussion started: 4 November 2026
© Author(s) 2026. CC BY 4.0 License.

With clay the soil clay content (%) and l the depth of soil layer and minimum Kd_{DOC} fixed at $10^{-1.5}$, and maximum Kd_{DOC} fixed at $10^{-3.2}$.

Only the free forms of DOC and of dHg can be degraded and mobilized from one pool to the other.

Vertical advection of DOC and dHg is modeled within the upper 2 meters of the soil profile,-a depth with explicit soil hydrology dynamic, and is linked to, but not directly proportional to, the rates of water percolation through the soil column. DOC and dHg transport via vertical water fluxes occurs in unfrozen soil layers and is governed by hydraulic conductivity, which is dynamically computed based on soil texture and temporally varying soil moisture (Guimberteau et al., 2018). Percolation is halted when the soil is entirely frozen, as ice-filled pores prevent water movement. To reflect the effects of heterogeneous subsoil textures and the presence of preferential flow pathways, a reduction factor is applied to vertical advection, limiting it to 20% of the corresponding water movement rate. This adjustment accounts for slower percolation and increased residence time within the soil (Bowring et al., 2019). Additionally, a 'poor-soil' module incorporates spatial heterogeneity by referencing a 0.5° resolution map of low-buffer-capacity soils, known for their limited ability to retain DOC, and thus dHg (Deluca and Boisvenue, 2012). In these "poor-soils" no reduction in vertical advection is applied. We assume that dHg and soil-Hg are closely bound to DOC and SOC, respectively, and are thus transported together. Therefore, vertical mixing of soil-Hg and dHg is directly proportional to that of their corresponding OC pools for each layer (l) (4):

$$soil - /dHg(l)_{after\ mixing} = soil - /dHg(l)_{before\ mixing} \times \frac{S/D - OC(l)_{after\ mixing}}{S/D - OC(l)_{before\ mixing}} \quad (4)$$

Vertical mixing of soil-Hg due to cryoturbation (downward movement of matter due to repeated freeze–thaw) in permafrost regions and bioturbation (by soil organisms) in non-permafrost regions are accounted for by adding a diffusion term following OC vertical mixing (Guimberteau et al., 2018) in the form of (5):

$$\frac{\delta Hg_i(z,t)}{\delta t} = I_{Hg(i)}(z,t) - g_i(z,t)\, Hg_i(z,t) + D \frac{\delta Hg^{\,2}{}_i(z,t)}{\delta z^{\,2}} \quad (5)$$

https://doi.org/10.5194/egusphere-2026-5859
Preprint. Discussion started: 4 November 2026
© Author(s) 2026. CC BY 4.0 License.

where Hg_i(z, t) is the solid content of Hg in pool *i* at depth *z* and time *t* (ng Hg m^{-3}); $I_{Hg(i)}$(z, t) the Hg input (ng Hg m^{-3} d^{-1}); g_i(z, t) the decomposition rate (d^{-1}); D the diffusive mixing rate, set as 10^{-3} m^2 yr^{-1} through the active layer, and decreases linearly to zero at 3 m in permafrost regions, to represent cryoturbative mixing (Koven et al., 2009), and is set as 10^{-4} m^2 yr^{-1} above 2 m in non-permafrost regions to represent bioturbation (Koven et al., 2013). The export of DOC and dHg from soil to river occurs via surface runoff and drainage. Dissolved substances are mobilized into surface runoff from the upper part of the soil column, specifically from the first five layers, corresponding to a cumulative source depth of approximately 4.5 cm. Drainage of DOC and dHg occurs from the 11th layer (1.5-2 m depth) and represents the deep export path over shallow groundwater. For the current version, we only consider export of DOC and dHg from the soil column via runoff and drainage, and leave the representation of coupled DOC and dHg cycling through the inland water network for future development.

2.2. Model forcing

External model input consists of meteorological forcing data , yearly landcover (PFTs) maps, yearly average atmospheric CO_2 concentrations, and monthly Hg deposition fluxes. Meteorological forcing data are derived from CRU-JRA v2.4 (University of East Anglia Climatic Research Unit et al., 2023) reanalysis at 3 hourly temporal and 2° (~200 km) spatial resolution. Atmospheric CO_2 data were used from TRENDY v2023 forcing data set (Sitch et al., 2024). Atmospheric Hg deposition fluxes were derived from GEOS-Chem v13.3.4 simulations at 2°×2.5° resolution, driven by MERRA-2 meteorological fields and the EDGAR anthropogenic emission inventory (Muntean et al., 2018) for 1970–2015. All forcing data were regridded to a common spatial resolution of 2° × 2° for the simulation. A pre-industrial GEOS-Chem simulation was also performed to provide deposition fields for the spin-up of terrestrial Hg pools in ORCHIDEE-Hg. The performance of this atmospheric Hg model has been extensively evaluated in previous studies (e.g., (Travnikov et al., 2017)). Here, we provide an evaluation of the specific model version used in this study against available observations (see Figs. A1 and A2).

https://doi.org/10.5194/egusphere-2026-5859
Preprint. Discussion started: 4 November 2026
© Author(s) 2026. CC BY 4.0 License.

Table 1: Data type, name, and sources of data files used to drive ORCHIDEE-Hg

Data type	Name	Initial spatial resolution	Source
Vegetation map	ESA CCI Land Cover dataset	0.25°	https://orchidas.lsce.ipsl.fr/dev/lccci/
Climatology	CRU-JRA v4.2	2°	CEDA Archive, (University of East Anglia Climatic Research Unit et al., 2023)
Atmospheric CO_2	Trendy v2023	global	Sitch et al., (2024)
Poor soils	Harmonized World Soil Database map	0.5°	Harmonized World Soil Database version 2.0, 2023
Hg deposition	GEOS-Chem v13.3.4	2 x 2.5°	https://zenodo.org/records/5764874

2.3. Simulation protocol

2.3.1. Spatial resolution

In this study, we conducted sub-continental simulations at 2° × 2°, which allowed us to cover the largest area with the smallest computational cost, although the model could be run at any spatial resolution with vegetation map and climatology data.

Vertical transport processes and especially cryo- bio-turbation which enhance the deep distribution of Hg and OC, require substantial computational resources, increasing simulation times by a factor of two to three. To reduce computational time, we limit simulations with vertical transport to a small simulation area (16–20°E, 53–55°N). Simulations over larger areas (e.g., 68-88°W, 30-50°N in North America and -10-26°E, 35-55°N in Europe, see Fig. 2 and paragraph 2.4.2 for rational) were run without cryo- and bio-turbation, and we estimated the amount of Hg and OC in each layer using proportional distribution determined over the small simulation area.

2.3.2. Temporal resolution and simulation duration

The full model operates with two different time steps: most OC and vegetation-related processes run at a daily time step; hydrological and energy related processes, as well as

https://doi.org/10.5194/egusphere-2026-5859
Preprint. Discussion started: 4 November 2026
© Author(s) 2026. CC BY 4.0 License.

litter, SOC, and Hg processes, run at a 30-minute time step. In this study, we used output files generated as yearly averages.

To reduce the computational burden of reaching equilibrium for SOC and soil-Hg, we employed a two-step spin-up approach, alternating between full model simulations and soil organic carbon and soil Hg module stabilization simulations. The full model was run from scratch for 80 years to allow the water cycle, vegetation growth, and litter C and Hg inputs to reach a pseudo-equilibrium state representative of pre-industrial period. Then, we forced the soil modules for OC and Hg in insulation at a daily time step for 3,000 years. We used fixed inputs, including litter OC and Hg input, fixed meteorological conditions and soil water content from the final year of the full model simulation period. A cycle of 40 years of full model runs followed by 3,000 years of soils C and Hg modules runs was repeated 8 times, covering a total simulation period of 24,440 years to reach equilibrium (see Fig. A3). This was followed by a final 80-year run of the full model to ensure consistency across all components.

The spin-up was run over the pre-industrial period using a loop of 20 years (1901–1920) of climate and CO_2 data of 1800, the first year (1800) of a prescribed vegetation map, and a 1-year loop of pre-industrial Hg fluxes (see Table 1).

Once all pools reached equilibrium, we ran historical simulations over the period 1900–2015 by updating the external forcing from the industrial to the present period. Climate, CO_2, and vegetation maps were updated starting from 1901, while Hg wet and dry deposition maps were updated from 1970 using per-industrial forcing for years before 1970.

2.4 Model evaluation

Model outputs are presented for Eastern North America and Europe. Evaluations were restricted to grid points with available evaluation data (Fig. A4, A5), *i.e.*, over the Eastern United States (US) and the European Union (EU). The EU area includes 4 grid points in the Iberian Peninsula with tropical forests (tropical broadleaf evergreen and tropical broadleaf raingreen forests, see Table A2) present at a very low coverage (~ 0.01 to 2% of the grid points). Outputs from these PFTs are used to evaluate Hg vegetation-mediated flux, but are

https://doi.org/10.5194/egusphere-2026-5859
Preprint. Discussion started: 4 November 2026
© Author(s) 2026. CC BY 4.0 License.

not considered reliable to evaluate the ecosystem Hg cycle (atmospheric sinks, soil re-emissions or soil storage) due to their very low coverage.

Model evaluation relies on assessing performance in terms of soil Hg stocks and sensitivity to environmental parameters. Evaluation was conducted against several observational datasets, including: Hg concentrations in vegetation, Hg litterfall and throughfall fluxes, digital maps of total soil Hg. Due to the lack of data on soil Hg evasion fluxes and time series of soil Hg, we focused on evaluating Hg inputs to soils (via litterfall and throughfall) as well as present-day stocks and concentrations. Given the strong dependency between Hg and C, we also performed model evaluation for Hg/C ratios. Detailed analysis of environmental factors (e.g., soil properties, atmospheric Hg deposition, climate) that may explain model biases will be the focus of a companion paper.

2.4.1. Output modeled variables

Model outputs are provided as yearly averages of fluxes (litterfall, throughfall, and soil re-emission) and stocks (litter OC, DOC, SOC, litter Hg, dHg, and soil-Hg). Vegetation-mediated fluxes such as litterfall and throughfall were analyzed for PFTs with LAI > 2. Hg concentrations in vegetation from model outputs were converted from ng $Hg \cdot gC^{-1}$ to ng $Hg \cdot g\ DM^{-1}$, assuming that vegetation dry matter (DM) consists of 50 % C (Matthews, 1997). Stocks and fluxes are analyzed both as PFT-weighted average based on the PFT coverage within each grid cell and per unit of the PFT area.

2.4.2. Evaluation dataset for model evaluation

Studies and associated variables used for the evaluation of the model are summarized in Table 2 and Figure 2 which illustrates their spatial coverage. The ORCHIDEE-Hg model was run over two reduced-size areas corresponding to regions with most available data for model evaluation: Eastern North America and continental Europe, see Figure 2.

Vegetation-related Hg variables, including Hg concentrations in different tissues, litterfall Hg fluxes, and throughfall Hg fluxes, were evaluated against the most up-to-date databases ((Sereni et al., 2026; Zhou and Obrist, 2021)) due to the lack of precision regarding tissue types or data used in global machine learning-based products (Wang et al., 2019). Given the spatial coverage of ORCHIDEE-Hg simulations, we limited the evaluation to 25°N–55°N

https://doi.org/10.5194/egusphere-2026-5859
Preprint. Discussion started: 4 November 2026
© Author(s) 2026. CC BY 4.0 License.

and excluded sites highly contaminated by anthropic activities from the observational datasets. These sites included locations near chlor-alkali industrial complexes, mining and gold-mining sites, combustion waste disposal sites, urban areas, and other impacted locations. Such sites were excluded because their elevated Hg concentrations are likely influenced by local or point sources that cannot be adequately represented at the spatial resolution of ORCHIDEE-Hg. In addition, to reduce the influence of extreme values potentially associated with localized anthropogenic contamination, we excluded outliers, defined as values outside of the 1.5 IQR (Chambers, 1998; Mcgill et al., 1978). .

Soil Hg is evaluated against large-scale soil surveys that provide spatially gridded maps of soil Hg concentrations. To ensure consistency, we first regridded the observation-based products to the model resolution (2° x 2°) through a bilinear interpolation regridding using the remapbil function of the cdo library (Schulzweida, 2019).

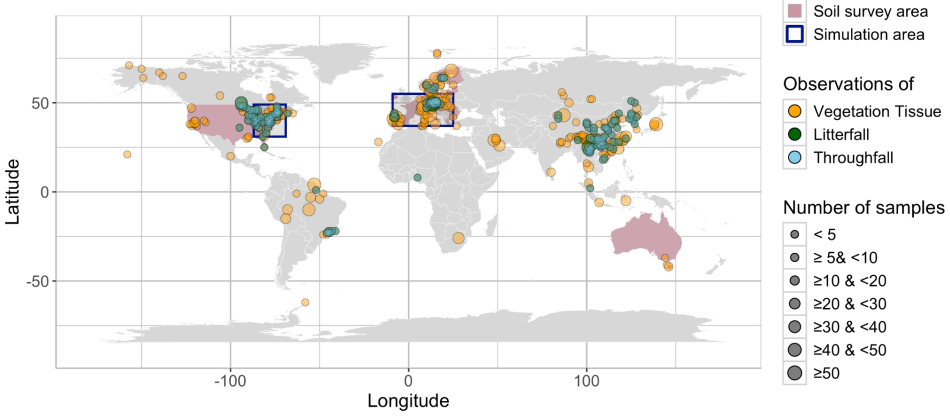


Figure 2: Map of available vegetation (Zhou and Obrist, 2021), litterfall, throughfall evaluation data from (Sereni et al., 2026) (symbolic points) and soil surveys with associated digital mapping evaluation data (colored area) (Ballabio et al., 2021; Olson et al., 2022). Square represents the area where simulations were run : 68-88°W, 30-50°N and -10-26°E, 35-55°N. Data availability on simulation areas is presented on Fig. A6 and per PFT in Table A3.

Table 2: Studies used for model evaluation including data type, spatial coverage and type of data (compilation from points measurement or survey and statistical mapping) with soil depth and spatial resolution when appropriate.

https://doi.org/10.5194/egusphere-2026-5859
Preprint. Discussion started: 4 November 2026
© Author(s) 2026. CC BY 4.0 License.

Data type	Study	Spatial coverage	Study type
Hg concentration in vegetation	Zhou et al., (2021)	Global	Compilation of observational data
Hg litterfall flux	Sereni et al., (2026)	Global	Compilation of observational data
Hg throughfall flux	Sereni et al., (2026)	Global	Compilation of observational data
Soil Hg	Olson et al., (2022) https://doi.org/10.1088/1748-9326/ac79c2	Conterminous United States	Survey and statistical mapping (0-5 cm for concentration, 0-100 cm for stocks) 3 x 3 km
	Ballabio et al., (2021)	European Union	Survey and statistical mapping (0-20 cm) 0.25 x 0.25 km
Soil OC	de Brogniez et al., (2015).	European Union	Survey and statistical mapping (0-20 cm) 0.25 x 0.25 km

Soil-related variables (e.g., water, OC, and Hg in litter, dissolved, and solid pools) are originally modeled as stocks (g m^{-2}) for each soil layer. Model evaluation is primarily performed against observational datasets derived from soil surveys, which generally report Hg concentrations over predefined depth intervals. Therefore, modeled Hg stocks are first converted into concentrations by computing bulk density-weighted averages over the corresponding depth interval according to Eq. (6):

$$\overline{[Hg]} = \frac{\sum_{l=1}^{n} Hg_l}{\sum_{l=1}^{n} BD_l L_l \times 1000} \quad (6),$$

where $\overline{[Hg]}$ is the mean Hg concentration (μg g^{-1} soil) over the depth interval encompassing layers (1) to (n), Hg_l is the Hg stock in layer l (ng m^{-2}), L_l is the thickness of layer (l) and BD_l is the bulk density of layer (l) (Harmonized World Soil Database version 2.0, 2023). The vertical soil profile follows an exponential distribution to account for the higher vertical

https://doi.org/10.5194/egusphere-2026-5859
Preprint. Discussion started: 4 November 2026
© Author(s) 2026. CC BY 4.0 License.

473 variability in the topsoil compared to deeper layers. Soil layer thickness ranges from 9.8 ×
474 10^{-4} m (for the first layer) to 3.7 m at a depth of 38 m. To align with survey data, we
475 compare 0–5 cm soil survey data to 0–4.5 cm modeled data, and 0–20 cm soil survey data
476 to 0–18.6 cm modeled data, using the closest model depths to the survey depths.

477 In addition to concentration-based comparisons, modeled Hg stocks were also directly
478 compared with observational Hg stocks whenever these were available from soil survey
479 products (Table 2). Such comparisons were considered complementary because
480 observational products provide both concentrations and stocks. In these cases, the
481 conversion from concentration to stock performed by the data providers is likely more
482 accurate than a conversion based on the global bulk density map used for model output
483 evaluation. The stocks and concentrations evaluations therefore provided an additional
484 means of assessing model performance while reducing uncertainties associated with bulk
485 density estimates. The number of data points used for evaluation in each of the simulation
486 areas is presented in Table A3.

487 Hg/C ratio analysis is restricted to Europe and does not include mountain areas >1000m
488 altitude that are masked in the OC observation product (de Brogniez et al., 2015).
489

490 **2.4.3. Evaluation procedure**

491 Model evaluation was conducted by comparing median and median absolute deviation
492 (MAD) rather than average of model and evaluation data to avoid bias due to highly
493 contaminated sites such as mining areas. The MAD is a robust measure of statistical
494 dispersion (Leys et al., 2013) calculated as (7):

495 $$MAD = c \times median(|x_i - median(x)|) \quad (7)$$

496 where c is a scaling constant set to $c=1/\Phi^{-1}(¾)= 1.48$. This value comes from the standard
497 normal distribution where Φ^{-1} is the inverse of the cumulative distribution function of a
498 standard normal variable. This scaling ensures that, for normally distributed data, the MAD
499 is consistent with the standard deviation (σ), allowing direct comparison between these
500 metrics (Huber, 1981, chap. 5).

https://doi.org/10.5194/egusphere-2026-5859
Preprint. Discussion started: 4 November 2026
© Author(s) 2026. CC BY 4.0 License.

We compute model residuals against evaluation data as the difference between evaluation data at the grid point *i* and model data at the grid point *i* (8):

$$residual_i = eval_i - mod_i \quad (8)$$

We used the mean absolute error (MAE) computed as (9):

$$MAE = \frac{\sum_{i=1}^{n} |eval_i - mod_i|}{n} \quad (9)$$

With $eval_i$ the value of evaluation data at the grid point *i*, mod_i the value of model value at the grid point *i* and *n* is the total number of grid points used for evaluation, because this metrics is less sensitive to outliers than the root mean square error (Willmott and Matsuura, 2005).

Model and evaluation data distribution were compared using Wilcoxon-Mann-Whitney with a significant test level at 0.05 (Mann and Whitney, 1947).

All statistical analysis and figures were done using R v.4.4.1 (R Core Team, 2024).

3. Results

3.1. Evaluation of Hg concentrations in vegetation compartments

3.1.1. Leaves Hg concentrations

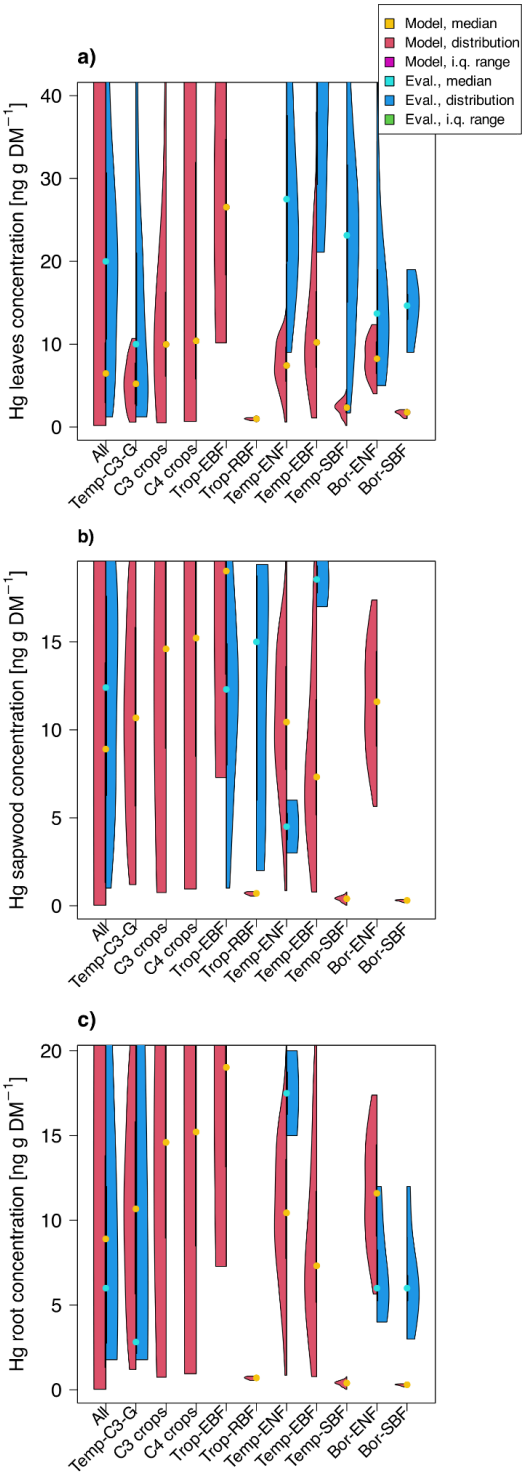
As shown in Fig. 3, modeled leaf Hg concentrations span a wide range, from 0 ng g^{-1} DM in a temperate broadleaf summergreen forest to 2713 ng g^{-1} DM in a C4 crop, with a median (± MAD) concentration of 7 ± 5 ng g^{-1} DM across all PFTs, and 90 % of the values below 30 ng g^{-1} DM (Fig. 3a and 3b).

When excluding outliers from the evaluation dataset, observed leaf Hg concentrations range from 1 ng g^{-1} DM in C3 grassland to 62 ng g^{-1} DM in temperate natural grassland, with a cross-PFT median (± MAD) of 20 ± 15 ng g^{-1} DM and 260 over 563 of the evaluation data within the simulations area. Median modeled leaf Hg concentrations are significantly different from observations (Wilcoxon-Mann-Whitney test p.v. < 10^{-16}) with modeled leaf Hg concentrations generally lower by a factor three than observed values for each of the PFTs (see Fig. 3a and 3b). However, this comparison is constrained by a limited evaluation

https://doi.org/10.5194/egusphere-2026-5859
Preprint. Discussion started: 4 November 2026
© Author(s) 2026. CC BY 4.0 License.

dataset for tropical evergreen broadleaf forest PFT represented by only one data point and for boreal summergreen broadleaf forest and the C4 grassland PFT represented only by four data points (see Table A2), introducing substantial uncertainty in the evaluations. Furthermore, most leaf samples were collected at the end of spring or early autumn, just before leaf fall, when Hg concentrations in leaves are typically at their annual maximum (Laacouri et al., 2013). In contrast, the model outputs represent annual averages, which integrate periods of both high and low Hg accumulation.

https://doi.org/10.5194/egusphere-2026-5859
Preprint. Discussion started: 4 November 2026
© Author(s) 2026. CC BY 4.0 License.



534

https://doi.org/10.5194/egusphere-2026-5859
Preprint. Discussion started: 4 November 2026
© Author(s) 2026. CC BY 4.0 License.

Figure 3: Annual Hg concentrations for the different PFTs represented in the simulated areas (red) compared to Hg concentrations from the evaluation dataset when available (Zhou and Obrist, 2021; blue): a) concentrations in leaves, b) concentrations in aboveground sapwood that include twigs, stem and sapwood tissue from the evaluation database, c) concentrations in roots. The number of sample or simulation grid points are indicated in Table A2. Temp-C3-G: temperate C3 grass; C3 crops: C3 crops; C4 crops: C4 crops; Trop-EBF: Tropical evergreen broadleaf forest; Trop-RBF: Tropical raingreen broadleaf forest; Temp-ENF: Temperate evergreen needleleaf forest; Temp-EBF: Temperate evergreen broadleaf forest; Temp-SBF: Temperate summergreen broadleaf forest; Bor-ENF: Boreal evergreen needleleaf forest; Bor-SBF: Boreal summergreen broadleaf forest.

3.1.2. Ligneous (trunk and root) tissues Hg concentrations

Modeled Hg concentrations in sapwood aboveground tissues range from 0 ng g^{-1} DM in a temperate broadleaf summergreen forest to 452 ng g^{-1} DM in a C4 crop, with a median (± MAD) of 9 ± 9 ng g^{-1} DM across all PFTs and 90% of the data below 19 ng g^{-1} DM, see Fig. 3b. Evaluation data for aboveground sapwood Hg concentrations range from 1 ng g^{-1} DM in tropical evergreen broadleaf forest, in tropical broadleaf raingreen forest and in temperate broadleaf summergreen forest to 34 ng g^{-1} DM in temperate broadleaf summergreen l forest, with a cross-PFT median (± MAD) of 13 ± 9 ng g^{-1} DM(see Fig. 3b). Across PFTs, the median modeled and observed Hg concentrations in sapwood aboveground tissues differ significantly (Wilcoxon-Mann-Whitney test, p. value=7 10^{-4}) with observed median Hg concentrations being approximately 1.5 times higher for PFTs with available observations but only 17 over 49 evaluation data within the simulation area.

Similarly, modeled Hg concentrations in root tissues range from 0. ng g^{-1} DM in a temperate broadleaf summergreen forest to 337 ng g^{-1} DM in a C4 crop, with a median (± MAD) of 9 ± 9 ng g^{-1} DM across all PFTs and 90% of the values below 19 ng g^{-1} DM, see Fig. 3c. Evaluation data for root Hg concentrations are extremely limited, with only 32 values available after excluding highly contaminated sites and 0 evaluation data within the simulation areas, see Table A2. Across PFTs, the median modeled and observed root Hg concentrations are not significantly different (Wilcoxon-Mann-Whitney test p. value =0.5) with observed root Hg concentrations ranging from 2 to 90 ng g^{-1} DM, with a median (± MAD) of 6 ± 6 ng g^{-1} DM across all PFTs, see Fig. 3c.

https://doi.org/10.5194/egusphere-2026-5859
Preprint. Discussion started: 4 November 2026
© Author(s) 2026. CC BY 4.0 License.

The limited availability of evaluation data for sapwood and root tissues constrains the robustness of the model evaluation at the PFT level. Nevertheless, median Hg concentrations are reasonably reproduced across all PFTs, with modeled values of the same order of magnitude as observational data.

3.2. Soil Hg inputs: litterfall and throughfall evaluation

Soil Hg inputs are modeled in three forms: wet Hg deposition on non-vegetated surfaces, litterfall flux following dry Hg uptake by vegetation and throughfall fluxes on vegetated surfaces.

3.2.a Litterfall Hg deposition

The median model litterfall Hg flux is 13 µg Hg m^{-2} yr^{-1} (MAD= 14) with the highest fluxes in southern US and from southwest to eastern Europe, where annual Hg litterfall fluxes reach 100-150 µg m^{-2} yr^{-1}, see Fig. A7.

Among PFTs, Hg litterfall fluxes are highest in boreal needleleaf forests (median ± MAD= 40 ± 16 µg Hg m^{-2} yr^{-1}; see Fig. 4). Overall, the modeled litterfall Hg flux is statistically different (Wilcoxon-Mann-Whitney test, p.value = 0.01) from the observed Hg litterfall flux from the evaluation dataset despite similar median (median ± MAD= 12 ± 5 µg Hg m^{-2} yr^{-1}). Modeled Hg litterfall flux was smaller than observation by a factor 3 to 4 for temperate summergreen forests. By contrast, modeled Hg litterfall fluxes were 2 to 3 times higher than observed Hg litterfall fluxes for evergreen temperate needleleaf and broadleaf forests, see Fig. 4.

https://doi.org/10.5194/egusphere-2026-5859
Preprint. Discussion started: 4 November 2026
© Author(s) 2026. CC BY 4.0 License.

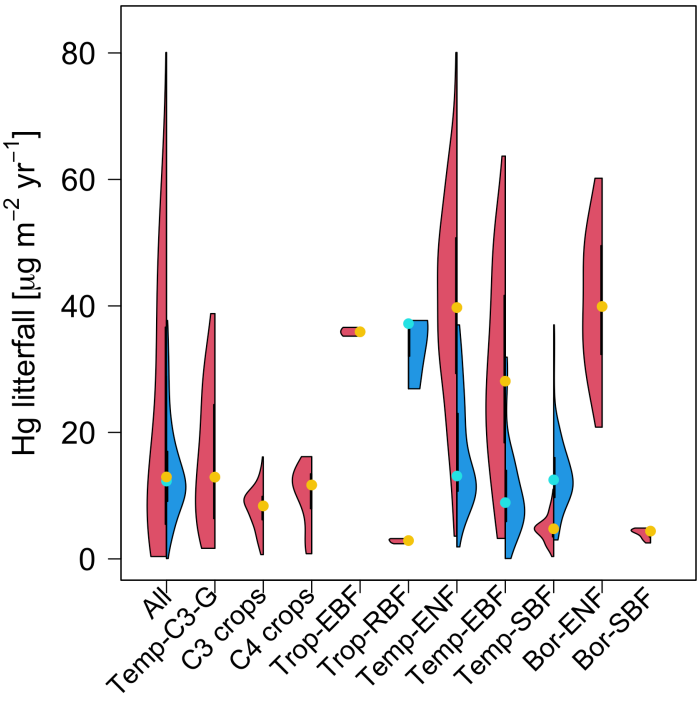


Figure 4: Litterfall annual mean Hg flux for the different PFTs represented in the simulated areas (red) compared to litterfall fluxes from the evaluation dataset when available (Sereni et al., 2026) (blue). The number of sample or simulation grid points are indicated in Table A2. Temp-C3-G: temperate C3 grass; C3 crops: C3 crops; C4 crops: C4 crops; Trop-EBF: Tropical evergreen broadleaf forest; Trop-RBF: Tropical raingreen broadleaf forest; Temp-ENF: Temperate evergreen needleleaf forest; Temp-EBF: Temperate evergreen broadleaf forest; Temp-SBF: Temperate summergreen broadleaf forest; Bor-ENF: Boreal evergreen needleleaf forest; Bor-SBF: Boreal summergreen broadleaf forest.

3.2.b. Throughfall flux: wet deposition on vegetated surfaces

Modeled Hg throughfall fluxes range from 2 to 12 µg Hg m^{-2} yr^{-1}, with a median (±MAD) of 6 ± 1 µg Hg m^{-2} yr^{-1}, see Fig. 5. Throughfall fluxes higher than 5 µg Hg m^{-2} yr^{-1} are modeled in the southern United States and central Europe (Germany), see Fig. A8. Modeled Hg throughfall fluxes differ significantly from observed median throughfall fluxes (Wilcoxon-Mann-Whitney test, p.v. <2 10^{-16}), being roughly 2 to 3 times lower than those in

https://doi.org/10.5194/egusphere-2026-5859
Preprint. Discussion started: 4 November 2026
© Author(s) 2026. CC BY 4.0 License.

the evaluation dataset, where the median (±MAD) flux is 12 ± 8 µg Hg m^{-2} yr^{-1} (Sereni et al., 2026) and where 63 over 149 evaluation data are within the simulation areas.

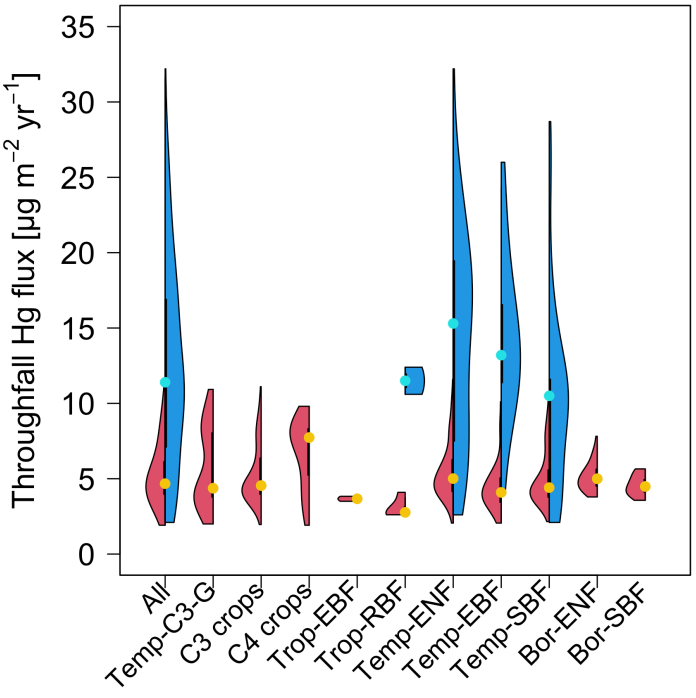


Figure 5: Throughfall annual mean Hg flux for the different PFTs represented in the simulation area (red) compared to throughfall flux from evaluation data (Sereni et al., 2026) (blue). The number of sample or simulation grid points are indicated in Table A2. Temp-C3-G: temperate C3 grass; C3 crops: C3 crops; C4 crops: C4 crops; Trop-EBF: Tropical evergreen broadleaf forest; Trop-RBF: Tropical raingreen broadleaf forest; Temp-ENF: Temperate evergreen needleleaf forest; Temp-EBF: Temperate evergreen broadleaf forest; Temp-SBF: Temperate summergreen broadleaf forest; Bor-ENF: Boreal evergreen needleleaf forest; Bor-SBF: Boreal summergreen broadleaf forest.

The modeled litterfall to throughfall ratio varied from 0 to 16 with median (± MAD)= 2 (± 3) L g^{-1} and differs significantly from the observed ratio (Wilcoxon-Mann-Whitney test p.v < 2 10^{-16}) but is in line with the order of magnitude (min, median= 1, max 4 L g^{-1} in the evaluation dataset), see Figs. A9 and A10. The consistency of the modeled litterfall to throughfall ratio demonstrates that our approach captures both dry deposition (via litterfall

https://doi.org/10.5194/egusphere-2026-5859
Preprint. Discussion started: 4 November 2026
© Author(s) 2026. CC BY 4.0 License.

flux) and wet deposition (via throughfall flux) weights, ensuring that their relative contributions are reliably represented across the simulated area.

3.3. Modeled soil Hg pools and emissions fluxes

3.3.1. Hg partitioning among pools and soil re-emission magnitude

The model includes theoretical Hg pools comprising four litter pools (two aboveground and two belowground), three soil pools, and seven dissolved Hg (dHg) pools. Across the top 2 m soil column, litter pools are substantially smaller than soil pools. Modeled Hg aboveground litter pools range from 0 to 4 g ha^{-1} (median ± MAD = 1 ± 1 g ha^{-1}), while modeled belowground litter pools range from 0 to 1 g ha^{-1} (median ± MAD = 0.2 ± 0.1 g ha^{-1}). In contrast, modeled soil Hg pools range from 15 to 390 g Hg ha^{-1}. Because the pools are conceptual constructs rather than measurable quantities, the simulated distribution of Hg among them cannot be directly evaluated against observations.

Among the three soil pools, the active Hg pool represents 0.1% to 0.6% of the total soil Hg pool, the slow Hg pool accounts for 21.7% to 33.0%, and the passive Hg pool constitutes 65.5 to 77.5% of the soil Hg pool, a partitioning comparable to that of SOC pools except for the active pool (Koven et al., 2015). dHg pools adsorbed to minerals represent less than 4 × 10^{-3} g Ha^{-1}, while free dHg pools range from 4 × 10^{-3} to 1 g Ha^{-1}, representing 2 to 17% of the soil Hg pool. When accounting for soil moisture, free dHg concentrations range from 1 to 98 ng L^{-1}, with a median ± MAD of 11 ± 8 ng L^{-1}, which aligns with values reported by Grigal, (2002) across various ecosystems. Yet, the lack of routing scheme in the current version of the model does not allow for comparison of Hg fluxes to streams or rivers, see Section 4.

Annual Hg^0 re-emissions range from 0 to 5 µg m^{-2} yr^{-1}(median ± MAD = 1 ± 2 µg m^{-2} yr^{-1}) for litter and from 1 to 14 µg m^{-2} yr^{-1} (median ± MAD = 4 ± 2 µg m^{-2} yr^{-1}) for soil pools, with a total median soil Hg re-emission of 5 µg m^{-2} yr^{-1} (range: 1 - 18 µg m^{-2} yr^{-1}, see Table A4). These values are consistent with observed soil Hg evasion fluxes reported in the literature (Blackwell et al., 2014; Jiskra et al., 2015) or modeled (Song et al., 2016). The smallest soil Hg emissions are modeled under boreal broadleaf summergreen forests, temperate broadleaf summergreen forests and tropical broadleaf raingreen forests while the highest are modeled for tropical broadleaf evergreen forests, see Table A4. Considering the

https://doi.org/10.5194/egusphere-2026-5859
Preprint. Discussion started: 4 November 2026
© Author(s) 2026. CC BY 4.0 License.

distribution of different PFTs, our model estimates global soil Hg^0 re-emissions at 648 Mg yr^{-1}, which aligns with recent lower estimates of soil Hg evasion ranging from 600 to 1367 Mg yr^{-1} (Obrist et al., 2018; Sonke et al., 2023).

3.3.2. Soil Hg vertical profile

Vertical profiles of Hg and OC from simulations including vertical transport (16–20°E, 53–55°N) are presented in Fig. A11 in terms of stock proportion per layer. In these simulations, 42% and ~77% of soil-Hg and SOC, respectively, are modeled in the first 4.5 cm (5 layers), while 75% and 82% of soil-Hg and SOC, respectively, are modeled in the first 18 cm (7 layers). The top 1 m contains 95% of soil-Hg and 92% of SOC, while soil-Hg and SOC stocks are zero in soil layers below 3 m and 2 m, respectively, reproducing the expected vertical gradient of decreasing Hg concentration with depth (Grimaldi et al., 2008; Ma et al., 2022; Richardson et al., 2013), but overestimating SOC stocks in the top layers by a factor of almost 2 (Jobbágy and Jackson, 2000). Accurately representing this vertical distribution is important because the depth at which Hg is stored influences its potential for downward transport, remobilization, and long-term sequestration in soils.

3.3.3. Spatial patterns of modeled soil Hg concentrations and stocks

Modeled soil Hg concentrations:

Over the 3 m soil column, modeled Hg soil concentrations range from 0 (25°E, 37°N (Cyprus, Greece)) to 9 μg kg^{-1} (-83 °W, 49°N (Ontario, Canada)) with a median (± MAD) of 2 ± 1 μg kg^{-1}. Modeled soil Hg concentrations are similar in range for the U.S. area (median ± MAD= 2 ± 1 μg kg^{-1}) and for the EU area (median ± MAD= 3 ± 1 μg kg^{-1}), see Fig. 6. The lowest Hg soil concentrations are modeled in southern Europe (Greece and Italy). The highest soil Hg concentrations are modeled in Canada, southern Georgia (US), and towards northeast Europe (Germany and Poland), which coincide with areas with the highest litterfall to throughfall ratios, see Fig. 6a and Fig. A9.

For the top 0-4.5 cm, modeled Hg soil concentrations ranged from 24 to 412 μg kg^{-1}. In the US area (±MAD), the median is 117 ± 44 μg kg^{-1} and in the EU area the median (± MAD) is 113 ± 65 μg kg^{-1}, see Fig. 6a. For the top 0-18.6 cm, modeled Hg soil concentrations ranged from 6 to 110 μg kg^{-1}, with a median of 31 ± 15 μg kg^{-1} in the US area and a median of 30 ± 17 μg kg^{-1} (± MAD) for the EU area, see Fig. 6d.

https://doi.org/10.5194/egusphere-2026-5859
Preprint. Discussion started: 4 November 2026
© Author(s) 2026. CC BY 4.0 License.

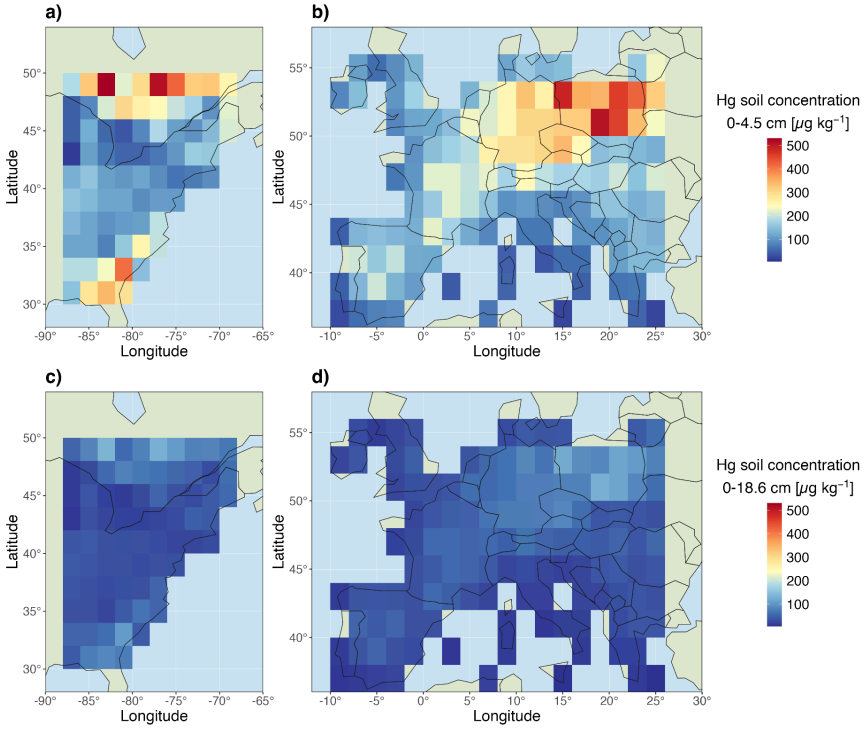


Figure 6: Modeled Hg soil concentration in µg Hg kg^{-1} soil for the 2 simulated areas (a), c), U.S. area; b), d), E.U. area) a), b) are the concentrations over 0-4.5 cm topsoil layers, c), d) are the concentrations over 0-18.6 cm topsoil layers.

Hg concentrations exceeding 50 µg kg^{-1} are modeled in temperate (median ± MAD = 72 ± 30 µg kg^{-1}) and boreal needleleaf evergreen forests (median ± MAD = 76 ± 25 µg kg^{-1}) ecosystems. Conversely, the lowest Hg concentrations are predicted for boreal broadleaf summergreen forests (median ± MAD = 19 ± 3 µg kg^{-1}), temperate broadleaf summergreen forests (median ± MAD = 22 ± 6 µg kg^{-1}), boreal needleleaf deciduous forest (median ± MAD = 20 ± 2 µg kg^{-1}) and C4 crops (median ± MAD = 22 ± 8 µg kg^{-1}) (see Table A4). These patterns are consistent with previous findings at local (Gruba et al., 2019; Richardson and Friedland, 2015) and continental scales (Ballabio et al., 2021), which report higher Hg concentrations in coniferous forests than in deciduous forests, as well as lower concentrations in agricultural and broadleaf ecosystems.

https://doi.org/10.5194/egusphere-2026-5859
Preprint. Discussion started: 4 November 2026
© Author(s) 2026. CC BY 4.0 License.

Modeled soil Hg stocks:

Over the 3 m soil column, Hg stocks ranged from 15 (15°E, 37°N Sicilia, Italy) to 390 (-77°E, 49°N Quebec, Canada) g ha^{-1} with a median of 100 ± 54 g Ha^{-1} (± MAD). 90 % of the modeled Hg soil stocks range between 33 and 257 g Ha^{-1}, see Fig. 7. Topsoil (0-18 cm) and 0-1m modeled Hg stocks are presented per area of simulations in the Table A5. By accounting for the global distribution of each PFT, we estimate global soil Hg stocks at 1139 Gg, with the largest stocks (261.0 Gg) occurring in tropical broadleaf evergreen forests and the smallest (0.3 Gg) in bare soils (see Table A5). Although our simulations do not include some ecosystems with specific Hg cycling, such as permafrost regions or tropical forests, our findings align with the highest estimates of soil Hg stocks in the 0–30 cm layer: 852–1265 Gg (based on measured Hg/C ratios, (Lim et al., 2020; Sonke et al., 2023)) and 709–1467 Gg (based on machine learning approaches, (Wang et al., 2019)).

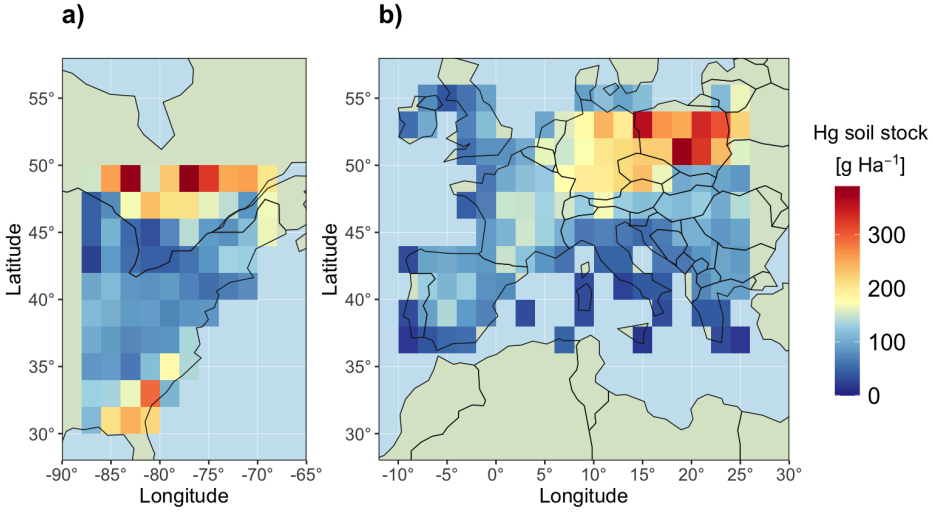


Figure 7: Modeled Hg stocks over the 3 m soil column, a) in the U.S. simulation area, b) in the E.U. simulation area

https://doi.org/10.5194/egusphere-2026-5859
Preprint. Discussion started: 4 November 2026
© Author(s) 2026. CC BY 4.0 License.

3.4. Evaluation of modeled soil Hg

3.4.1. Median-based evaluation of modeled Hg soil concentrations and stocks.

From evaluation data, soil Hg concentrations in the U.S. (0–5 cm layer) range from 17 to 176 µg kg^{-1}, with 90% of values < 128 µg kg^{-1} (median ± MAD = 34 ± 20 µg kg^{-1}). In the EU (0–20 cm layer), they range from 8 to 379 µg kg^{-1}, with 90% of values < 90 µg kg^{-1} (median ± MAD = 35 ± 23 µg kg^{-1}).

Over the two simulation areas, modeled Hg concentrations are significantly different (Wilcoxon-Mann-Whitney test, p.value =$9x10^{-3}$) but on the order of magnitude of the evaluation data set, see Fig. 8a. However, simulated Hg concentrations are higher than evaluation data in the U.S. area but lower in the EU area, see Fig. 8b. Yet, in the U.S. and EU areas, 0% and 80%, respectively, of modeled grid point concentrations fall within their respective evaluation dataset MAD.

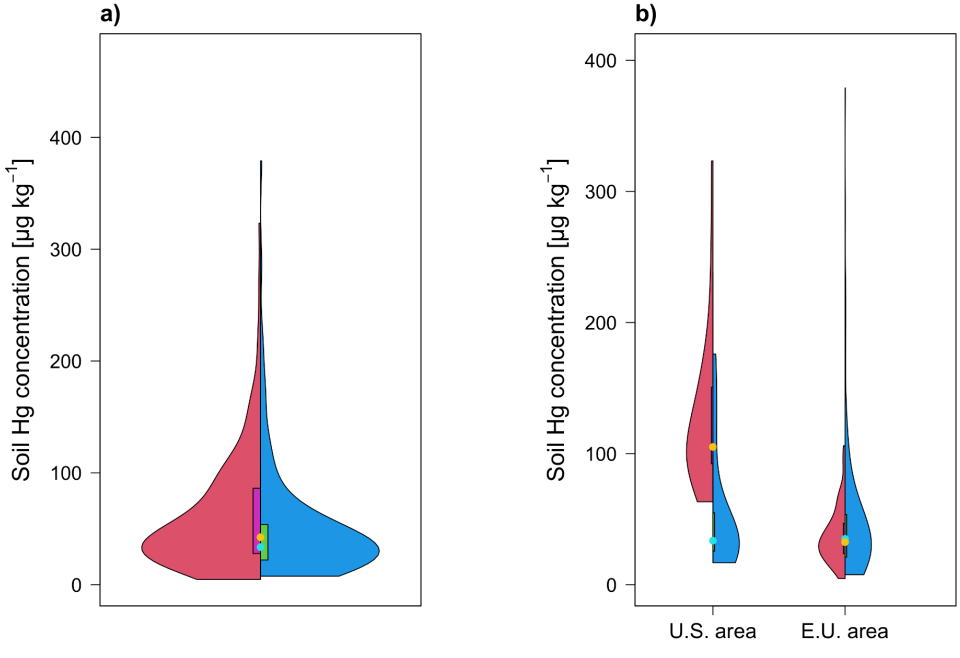


Figure 8: Comparison of modeled and observed soil Hg concentrations. a) Hg soil concentrations concatenated across both U.S. and Europe simulation areas. b) Hg soil concentrations displayed as separate violin plots for each simulation area. For the U.S. area,

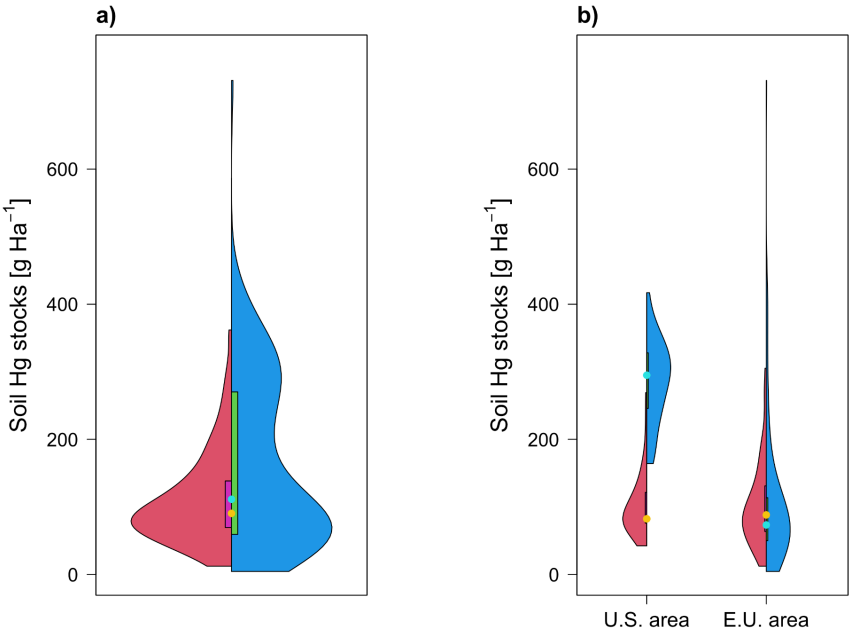
https://doi.org/10.5194/egusphere-2026-5859
Preprint. Discussion started: 4 November 2026
© Author(s) 2026. CC BY 4.0 License.

the presented Hg concentrations are in top 4.5 cm and 5.0 cm soil layers, respectively. In Europe, the compared Hg concentrations are in top 18.6 cm and 20 cm soil layers, respectively. The number of points are indicated in Table A4.

Soil Hg stocks from the evaluation dataset range from 164 to 417 g ha^{-1} (with 90% of values < 351 g ha^{-1}; median ± MAD = 295 ± 58 g Ha^{-1}) in the 0–1 m soil column in the U.S. area. In the EU area, observed stocks range from 5 to 731 g ha^{-1} (with 90% of values < 216 g ha^{-1}; median ± MAD = 73 ± 45 g Ha^{-1}) in the 0–20 cm soil column. With our estimation of ~75% of stocks in the 0–20 cm layer, Hg stocks in the U.S. evaluation dataset are roughly three times larger than those in the EU dataset, despite the highest concentration values in the EU evaluation dataset .

Across the two simulation areas, modeled Hg stocks differ significantly from those in the evaluation dataset (Wilcoxon-Mann-Whitney test, p. value= 0.01), see Fig. 9a. Modeled Hg stocks are lower than the evaluation dataset in the U.S. but higher in the EU, see Fig. 9b. Furthermore, only 2% of modeled grid-cellHg concentrations in the U.S. fall within the MAD of the U.S evaluation dataset, compared with 63% in the EU.

https://doi.org/10.5194/egusphere-2026-5859
Preprint. Discussion started: 4 November 2026
© Author(s) 2026. CC BY 4.0 License.



746

747 **Figure 9**: Modeled and evaluated Hg soil stocks respectively for modeled and observation
748 0-4.5 cm and 0-100 cm for U.S. area, 0–18.6 cm, 0-20 cm for E.U. area. a) Hg soil
749 concentrations concatenated across both simulation areas. b) Hg soil concentrations
750 displayed as separate violin plots for each simulation area. The number of points used for
751 evaluation are indicated in Table A4.

752 Part of the mismatch with U.S. stocks between our model and the evaluation dataset could
753 be related to the SOC vertical profiles. Indeed, Olson et al. (2022) report comparable Hg
754 concentrations between 20 cm and 1 m depth, thus implying higher Hg stocks over the 0 - 1
755 m soil column, whereas our simulated concentrations decrease by approximately 50% over
756 this depth range in agreement with the vertical SOC profile for various soils types (Grimaldi
757 et al., 2008; Ma et al., 2022; Richardson et al., 2013).

758 **3.4.2. Grid point residuals analysis**

759 *3.4.2.a. Hg concentrations residuals*

760 Over the two simulations, Hg concentration residuals (observation - model) range from
761 -304 to 364 µg kg^{-1} (median ± MAD = -8 ± 45 µg kg^{-1}). The absolute maximum residual value

https://doi.org/10.5194/egusphere-2026-5859
Preprint. Discussion started: 4 November 2026
© Author(s) 2026. CC BY 4.0 License.

is 249 µg kg^{-1}, after excluding the more concentrated evaluation data point situated at 11°E, 43°N, where Ballabio et al., (2021) already identified the very highly contaminated site of Mt Amiata. In the U.S. area, ~12% of the modeled Hg concentrations are underestimated, with a median residual of -62 ± 43 µg kg^{-1} and a MAE of 86 µg kg^{-1} . In the EU area, ~54% of the modeled Hg concentrations are underestimated, with a median residual of 6.4 ± 32 µg kg^{-1} and a MAE of 36 µg kg^{-1}, see Fig. 10a. Compared with the dispersion of the evaluation data, 38% of the model residuals fall within the observation ± MAD range (53% within the ±1.5 MAD interval). This indicates that the model performes relatively well with a bias of the same order of magnitude as the evaluation data range, except for highly contaminated points (soil Hg concentration > 200 µg kg^{-1}); see Fig. 10a.

3.4.2.b Hg stocks residuals

Hg stock residuals range from -280 to 693 g ha^{-1} (median ± MAD = 42 ± 139 g Ha^{-1}), with an absolute maximum value of 344 g ha^{-1} after excluding the 11°E, 43°N grid point. In the U.S. area, modeled Hg stocks are consistently underestimated, with a median residual of 186 ± 64 g ha^{-1} and a MAE of 182 g ha^{-1}. In the EU area, residuals are roughly equally distributed between under- and overestimation, with a 1st quartile of -58 g Ha^{-1}, a median of -1 g Ha^{-1}, a 3rd quartile of 44 g Ha^{-1}, and a MAE of 82 g Ha^{-1}. Across the two simulations, 42% of the residuals lie within the ± MAD interval of the evaluation data, but from the U.S. area output, only 2% are within this range due to the large 0–1 m stocks in the evaluation dataset, see Fig. 10b.

Although our model's MAE is comparable to median soil Hg concentrations, its performance remains consistent with that of reference evaluation products. For instance, Ballabio et al. (2021) kriged residuals from a Hg gridded product over the EU predominantly fall within the -60 to -6 µg kg^{-1} range or within the 1 to 38 µg kg^{-1} range, compared to a median Hg concentration (excluding hotspots) of 38 µg kg^{-1}. Besides, even with an extensive set of tested variables, the authors could not account for the high concentrations observed in 58% of the Hg hotspots, highlighting the difficulty in representing multi-source point contamination sites.

https://doi.org/10.5194/egusphere-2026-5859
Preprint. Discussion started: 4 November 2026
© Author(s) 2026. CC BY 4.0 License.

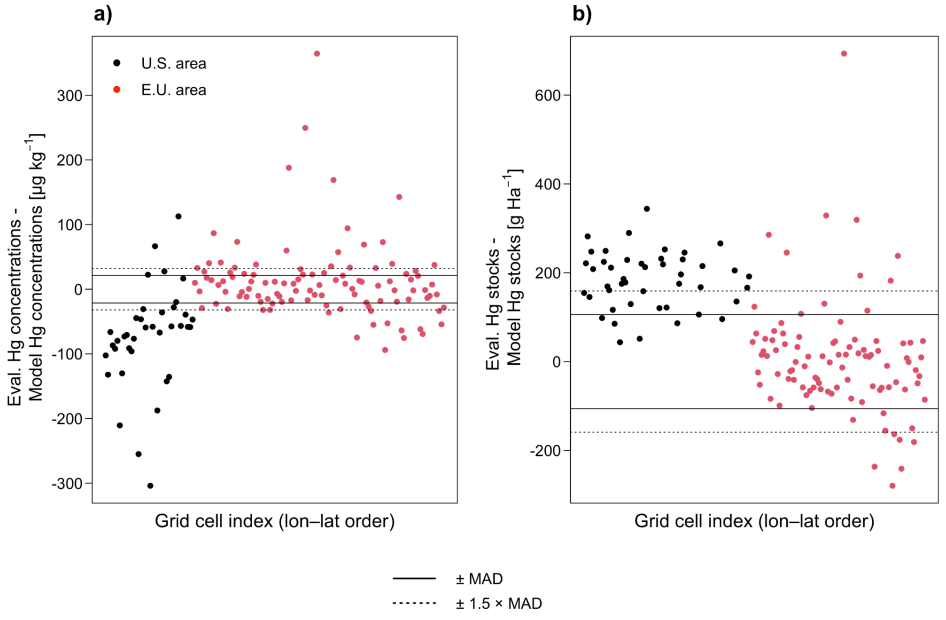


Figure 10: Residuals of Hg concentrations (a) expressed in µg kg^{-1} and stocks (b) expressed in g Ha^{-1} for the two simulations area (U.S. in black, E.U. in red). ± MAD of evaluation data and ± 1.5 MAD of the evaluation dataset are represented to scale residuals. The number of points used for evaluation are indicated in Table A4.

Further exploration of the potential environmental drivers of these biases will be conducted in a second, companion, study. Given the tight coupling of the Hg and C cycles in ORCHIDEE-Hg v1.0, we complement our evaluation by examining Hg/C ratios as an additional metric.

3.4.3. Evaluation of modeled Hg/C

Simulated Hg/C ratios of the top 0-20 cm ranges from 0.2 µg g^{-1} in -9°E, 43°N, Galicia, Spain to 3 µg g^{-1} in -5°E; 41°N, Castile and Léon, Spain with median (± MAD)= 1 (± 0.5 µg g^{-1}), see Fig. A13a.

The Hg/C ratio of the evaluation dataset ranges from 0.06 µg g^{-1} in -3°E, 41°N, Guadalajara, Spain to 10.9 µg g^{-1} in -5°E, 39°N Hg mining in Estrémadure, Spain with median (±MAD)= 1.06 (+- 0.66) µg g^{-1}, see Fig. A13b.

https://doi.org/10.5194/egusphere-2026-5859
Preprint. Discussion started: 4 November 2026
© Author(s) 2026. CC BY 4.0 License.

Overall, the model reproduces the observed range of Hg/C ratios reasonably well, with 55 % of simulated values falling within the evaluation dataset MAD and 67% within 1.5 MAD (see Fig. A14), indicating a generally consistent representation of Hg-C associations in soils.

4. Discussion

4.1. Limitations of evaluation dataset

Our study presents ORCHIDEE-Hg v1.0, the first mechanistic ecosystem Hg model to be extensively evaluated against both fluxes (litterfall, throughfall) and soil Hg observational datasets. Although the evaluation was primarily limited to temperate regions with available datasets, the model reproduces median values of litterfall, throughfall fluxes and soil Hg stocks of observational databases. However, the lack of observation of Hg concentration and litterfall flux for uncontaminated sites across several PFTs, such as croplands and grasslands, limited our evaluation to forest ecosystems. Furthermore, the scarcity of observations of Hg concentrations in roots and trunks limited the robustness of our evaluation, despite the critical role of woody tissues in accurately representing vegetation Hg stocks their response to environmental changes, including land use change and forest fires.

The spatial and temporal resolution of the evaluation databases introduce additional limitations. We simulated regions for which a large number of vegetation and concentration data points are available (see Fig. 2) but we evaluated the model against all available data from uncontaminated sites, including data from East Asia and South America to cover as many PFTs as possible. This introduces potential biases, as the environmental drivers of litterfall and vegetation Hg concentrations (*e.g.*, temperature, evapotranspiration and soil moisture, wind speed(Chen et al., 2024b; Jia et al., 2026)) may differ significantly between these regions, leading to mismatches in model-performance comparisons.

We chose to conduct soil Hg evaluation against regional gridded observational products for two reasons. First, this ensures a common sampling and interpolation procedure for each continental area, and second, it allows point-to-point comparisons. However, by derivating high resolution maps from soil sampling and auxiliary covariates, gridded products can introduce supplementary bias. For instance, comparison of two observational products

https://doi.org/10.5194/egusphere-2026-5859
Preprint. Discussion started: 4 November 2026
© Author(s) 2026. CC BY 4.0 License.

across Europe (GEMAS (Reimann et al., 2018) and LUCAS (Ballabio et al., 2021)) reveals significant discrepancies in spatial patterns: in Scandinavia, Ballabio et al.'s (2021) observational product shows a strong Hg anomaly, while Reimann et al., (2018) depict a low background. Similarly, Reimann et al. (2018) show patches of high concentrations in central Germany and western Austria, while Ballabio et al., (2021) predict a larger area of higher concentrations from northern Italy to Germany. However, positive residuals in Ballabio's product, indicating underestimation of Hg concentrations, align with our own findings in regions such as Northern Spain, mining areas, the United Kingdom, and Italy. This highlights that even the highly parametrized statistical model used to construct observation products underestimated Hg concentrations in these regions, without identifying clear missing factors in nearly half of the cases.

4.2. Current model limitations and parametrization gaps

Vegetation Hg concentrations:

For the first time, plant woody tissues and roots are explicitly represented in a large-scale Hg model, and simulations capture observed patterns reasonably well (see Fig. 3). This approach allows us to estimate Hg concentrations in woody tissue and litterfall. However, the current parameterization remains oversimplified in several respects. First, only leaf Hg uptake is mechanistically parameterized, while Hg concentrations in other tissues are estimated as a proportion (which can exceed 1) of leaf Hg. Furthermore, due to data constraints (e.g., some PFTs have observations only for twigs), heartwood and sapwood and fruits, reserve carbon, and leaves are grouped together.

Then, the current framework does not account for progressive tree growth. By explicitly accumulating only leaf Hg and computing branch, trunk, or root Hg as a proportion of leaf Hg, the model assumes that an abrupt increase in atmospheric Hg concentrations immediately affects the entire tree. In reality, only the most recent tree ring should reflect such changes, as Hg uptake occurs over time. This is critical for accurately capturing Hg transfer to litter pools, which are essential when designing future scenarios.

Finally, the vegetation Hg uptake parameterization is based on observations from a single deciduous forest in the U.S. (Rea et al., 2002) and currently only accounts for LAI and Hg dry

https://doi.org/10.5194/egusphere-2026-5859
Preprint. Discussion started: 4 November 2026
© Author(s) 2026. CC BY 4.0 License.

deposition fluxes, neglecting variations in plant uptake capacity in response to environmental factors such as atmospheric CO_2, temperature, leaf age, or plant type (Chen et al., 2024b; Jia et al., 2026; Zhou et al., 2021). Future scenarios will incorporate changes in CO_2, temperature, precipitation, and other drivers. Therefore, their explicit inclusion in ORCHIDEE-Hg is essential to accurately simulate evolving plant Hg uptake and, consequently, to establish robust Hg cycling projections. Additionally, PFT-specific parameterization of atmospheric Hg uptake should be developed to capture processes such as needle-specific processes. However, the multiplicity and non-linearity of environmental drivers of leaf Hg uptake significantly hinder our ability to represent these processes in a mechanistic model (Jia et al., 2026).

Soil processes:

The proposed model parameterization successfully reproduces soil Hg stocks across the U.S. and EU by linking soil Hg dynamics to soil OC dynamics. Yet, while this coupling allows us to leverage the numerous developments in soil processes, it also introduces a strong dependency of the model's OC performance, both in terms of environmental drivers and pool kinetics. Besides, to account for reduced Hg^0 evasion compared to soil OC decomposition, we introduced fd_{Hg}. However, this parameter was fitted using a single value based on the European Hg/C ratio, raising questions about whether all Hg pools share the same affinity for different OC pools. Given that fd_{Hg} governs the partitioning of Hg between pools with different turnover times, the sensitivity and relaxation time of soil Hg are highly dependent on its value. Yet, the conceptual nature of the pools, combined with the very long turnover times of slow and passive pools, makes direct calibration based on re-emission fluxes challenging. Therefore, extensive sensitivity testing must be conducted before any prospective simulations to ensure robust projections of soil Hg dynamics.

4.3. Potential applications of ORCHIDEE-Hg

ORCHIDEE-Hg v1.0 is directly based on the land surface model ORCHIDEE. This framework facilitates future integration of advanced developments regarding *e.g.*, the routing of dissolved species (Bowring et al., 2019), erosion and transport of particulate species (Zhang et al., 2022), effects of forest fires on biogeochemical cycling (Yue et al., 2013, 2015), improved representation of vegetation dynamics by forest age cohorts (Yue et al., 2018), or

https://doi.org/10.5194/egusphere-2026-5859
Preprint. Discussion started: 4 November 2026
© Author(s) 2026. CC BY 4.0 License.

parametrisation of new PFTs such as lichen and mosses (Druel et al., 2017), mangroves (Zhao et al., 2025) or peatland vegetation (Qiu et al., 2026).

Besides, this integration unlocks the complete toolkit to investigate the interconnected impacts of climate variability, land-use changes, and vegetation type distributions. It allows for analysis of how environmental drivers influence soil OC stability, thus Hg retention in soils, as well as the Hg cycle itself, including critical processes such as vegetation uptake and litterfall deposition. Furthermore, ORCHIDEE-Hg is the first terrestrial Hg model to produce an explicit Hg budget integrated across vegetation, soil, atmosphere, and inland waters by explicitly representing dissolved Hg species in soil solution, although their routing to rivers is not yet included. Furthermore, while not explored in this work, the model incorporates fire parameterizations that will enable future estimation of Hg emissions to air, particularly through the combustion of Hg stored in woody tissues, thereby closing an important gap in the representation of Hg fluxes between terrestrial ecosystems and the atmosphere.

5. Conclusion

This study introduces ORCHIDEE-Hg v.1.0, a process-based terrestrial Hg model evaluated against observations across large temperate regions. We demonstrate its ability to reproduce patterns of Hg deposition and soil Hg stocks at the regional to continental scale. While the current framework does not yet account for permafrost regions or mining hotspots, we estimate global Hg soil re-emissions of 648 Mg yr^{-1} and global soil Hg stocks of 1138 Gg, providing a baseline for investigating Hg dynamics at the global scale.

By establishing this baseline, this work provides a foundation for further investigation of environmental drivers and parametric uncertainties. The next evaluation steps, conducted in a companion paper, will examine model sensitivity to atmospheric Hg deposition, environmental factors, and key parameters such as fd_{Hg}. This analysis will help identify the parameters that control short- and long-term soil Hg storage and improve projections of soil Hg stock evolution under changing environmental conditions.

https://doi.org/10.5194/egusphere-2026-5859
Preprint. Discussion started: 4 November 2026
© Author(s) 2026. CC BY 4.0 License.

6. Appendix

Table A1: Allocation parameter of Hg in ligneous tissues for the different plant functional types (PFT) derived from (Zhou and Obrist, 2021), table 1), k_{alloc_ba} allocation coefficient for aboveground brown tissues (aboveground sapwood, aboveground heartwood) and k_{alloc_bb} allocation coefficient for belowground brown tissues (belowground sapwood, belowground heartwood and roots).

PFT	k_{alloc_ba}	k_{alloc_bb}
Tropical broadleaf evergreen forest	0.23	0.71
Tropical broadleaf raingreen forest	0.23	0.71
Temperate needleleaf evergreen forest	0.59	1.4
Temperate broadleaf evergreen forest	0.23	0.71
Temperate broadleaf summergreen forest	0.29	0.17
Boreal needleleaf evergreen forest	0.59	1.4
Boreal needleleaf deciduous forest	0.29	0.17
Boreal broadleaf summergreen forest	0.38	0
Boreal needleleaf deciduous forest	0	2.1
Temperate natural grassland C3	0	2.1
Natural grassland C4	0.75	1.5
Crops C3	0.75	1.5
Crops C4	0.75	1.5

https://doi.org/10.5194/egusphere-2026-5859
Preprint. Discussion started: 4 November 2026
© Author(s) 2026. CC BY 4.0 License.

Tropical natural grassland C3	0.31	1.0
Boreal natural grassland C3	0.27	0.6

Table A2: Number of data points per plant functional type (PFT): model output (N model) and evaluation data (N eval.) for Hg concentrations ([Hg]) in vegetation tissues, litterfall fluxes, and litterfall/throughfall ratios. Spatial coverage of the different PFTs can be found in https://orchidas.lsce.ipsl.fr/dev/lccci/ as indicated in Table 1.

PFT	N. model	N eval. leaves [Hg]	N eval. sapwood [Hg]	N eval. roots [Hg]	N eval. litterfall Hg flux	N eval. Hg throughfall flux	N eval. litterfall Hg / throughfall Hg
Tropical broadleaf evergreen forest	2	1	-	-	2	1	1
Tropical broadleaf raingreen forest	4	-	7	-	3	2	
Temperate needleleaf evergreen forest	201	61	2	2	113	69	48
Temperate broadleaf	55	8	2	-	61	16	13

https://doi.org/10.5194/egusphere-2026-5859
Preprint. Discussion started: 4 November 2026
© Author(s) 2026. CC BY 4.0 License.

evergreen forest							
Temperate broadleaf summergreen forest	130	242	8	1	192	54	40
Boreal needleleaf evergreen forest	42	38	-	6	-		-
Boreal broadleaf summergreen forest	14	4	-	6	-		-
Temperate natural grassland (C3)	37	129	-	17	-	1	-
C3 Crop	115	-	-	-	-	-	-
C4 Crop	28	-	-	-	-	-	-
Total	628	495	49	32	377	107	149

https://doi.org/10.5194/egusphere-2026-5859
Preprint. Discussion started: 4 November 2026
© Author(s) 2026. CC BY 4.0 License.

943

944

945 **Table A3**: Number of soil grid points modeled and used for evaluation

946

	Number of modeled grid points	Number of Hg concentrations evaluation grid points	Number of Hg stocks evaluation grid points
U.S. area	100	38	45
EU area	177	97	97

947

948 **Table A4**: Median soil Hg stocks (0-38m) and soil Hg^0 evasion flux per m^2 of PFT and
949 estimated soil Hg stocks (0- 38m) and soil Hg^0 evasion flux at the global scale in respect with
950 PFT spatial coverage.

951

PFT	Surface of PFT [Mkm^2]	Median soil Hg [$mg\ m^{-2}$]	Median soil Hg evasion [$ng\ h^{-1}$]	Soil Hg stocks [Gg]	Soil Hg^0 evasion [$Mg\ yr^{-1}$]
Bare soil	29.6	0.1	0.0	0.3	0.0
Tropical broadleaf evergreen forest	14.6	178.6	1.6	261.0	205.2
Tropical broadleaf raingreen forest	8.5	62.4	0.4	53.1	29.2

https://doi.org/10.5194/egusphere-2026-5859
Preprint. Discussion started: 4 November 2026
© Author(s) 2026. CC BY 4.0 License.

Temperate needleleaf evergreen forest	6.5	2375	1,5	153.2	83.5
Temperate broadleaf evergreen forest	3.3	139.2	1.1	46.4	31.9
Temperate broadleaf summergreen forest	7.3	72.5	0.3	52.9	22.2
Boreal broadleaf summergreen forest	3.3	61.5	0.3	20.4	9.9
Boreal needleleaf evergreen forest	6.8	254.6	1.4	173.0	82.9
Temperate natural C3 grassland forest	9.3	120.5	0.9	112.2	75.8
C3 Crop	16.5	814	0.6	134.2	82.0
C4 Crop	4.4	69.5	0.7	30.9	25.7
Total	144.1	79.0	0.5	1138.7	640.0

https://doi.org/10.5194/egusphere-2026-5859
Preprint. Discussion started: 4 November 2026
© Author(s) 2026. CC BY 4.0 License.

Table A5: Statistical description (min, median, max and median average deviation (mad)) of depth aggregated Hg soil stocks in g Ha^{-1} for the two simulations area.

	Hg stocks 0 - 18cm				Hg stocks 0 - 75 cm				Hg stocks 0 - 38 m			
	min	median	mad	max	min	median	mad	max	min	median	mad	max
U.S. area	19.1	82.3	39.9	307.8	23.0	99.4	48.4	371.4	24.1	104.3	50.8	389.8
EU area	11.9	78.3	42.3	300.4	14.4	94.5	50.9	362.5	15.1	99.1	52.4	380.4

https://doi.org/10.5194/egusphere-2026-5859
Preprint. Discussion started: 4 November 2026
© Author(s) 2026. CC BY 4.0 License.

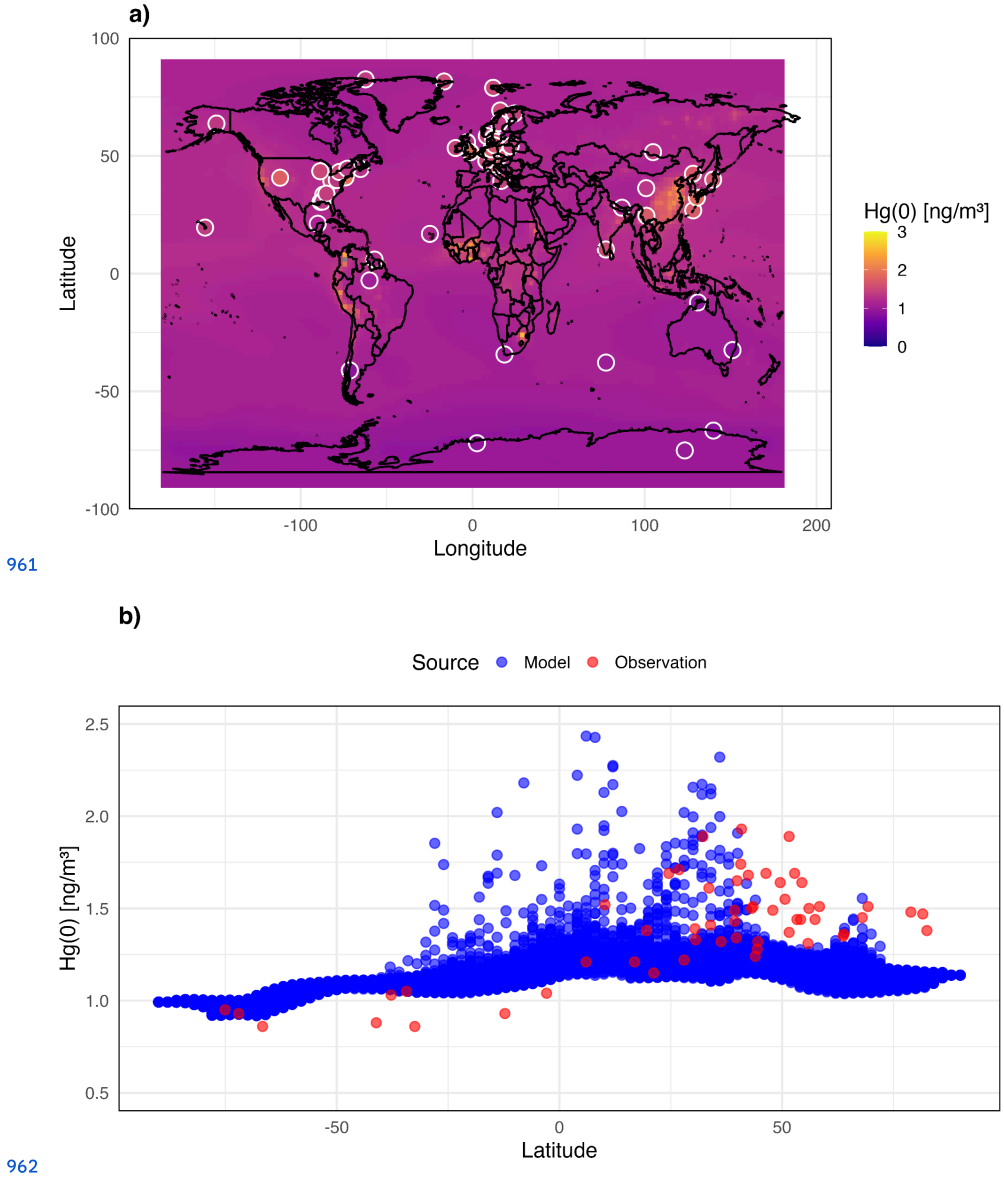
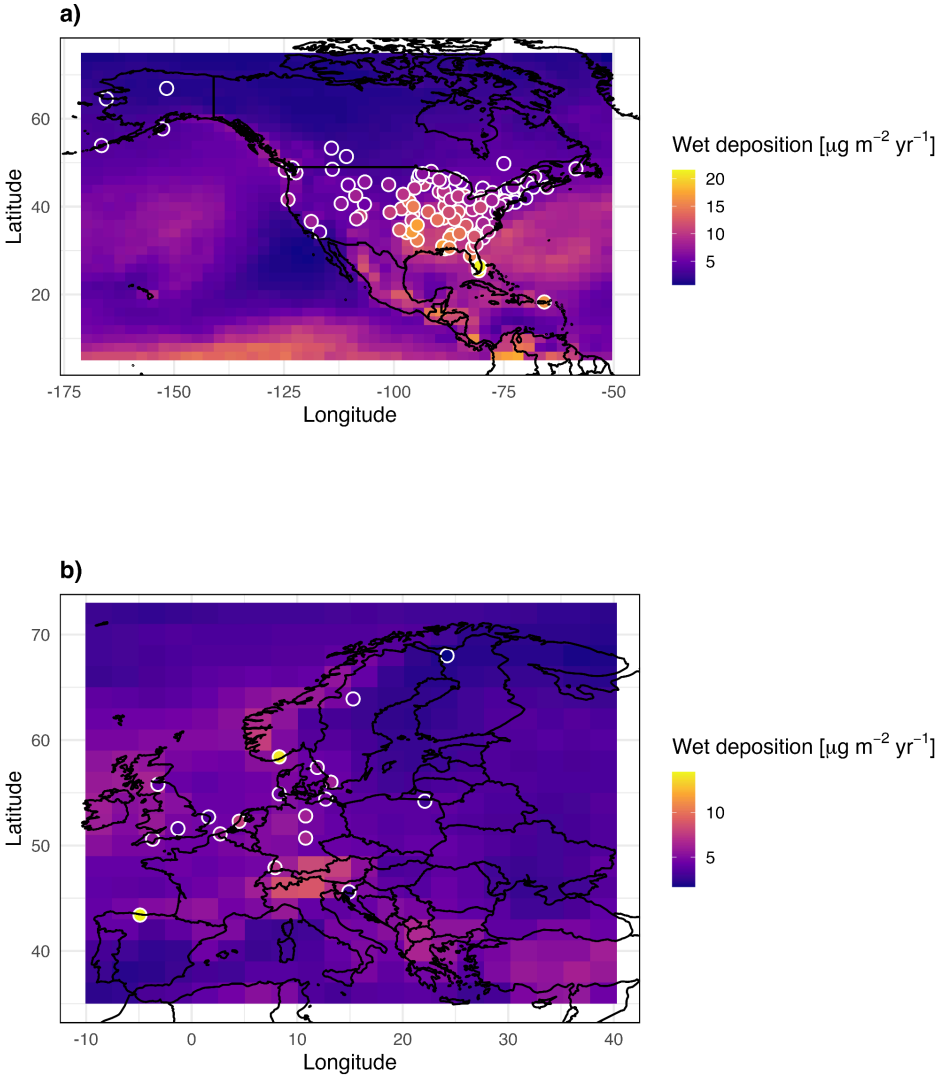


Figure A1: Spatial and latitudinal comparison of modeled and observed atmospheric Hg(0) concentrations. a) Spatial distribution of modeled Hg(0) concentrations (color shading; year 2015) and observed concentrations (circles; 2013–2015 average). b) Modeled and observed Hg(0) concentrations as a function of latitude, with model results and observations shown in blue and red, respectively.

https://doi.org/10.5194/egusphere-2026-5859
Preprint. Discussion started: 4 November 2026
© Author(s) 2026. CC BY 4.0 License.



969

970

971

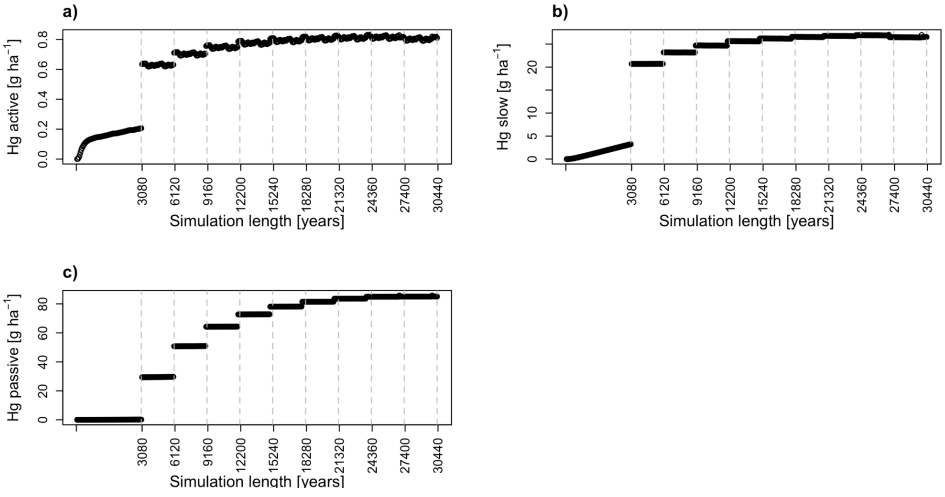
972 **Figure A2:** Spatial distribution of modeled and observed atmospheric Hg wet deposition
973 fluxes (year 2015). Color shading represents modeled wet deposition fluxes while circles
974 indicate observed values.

975

976

https://doi.org/10.5194/egusphere-2026-5859
Preprint. Discussion started: 4 November 2026
© Author(s) 2026. CC BY 4.0 License.

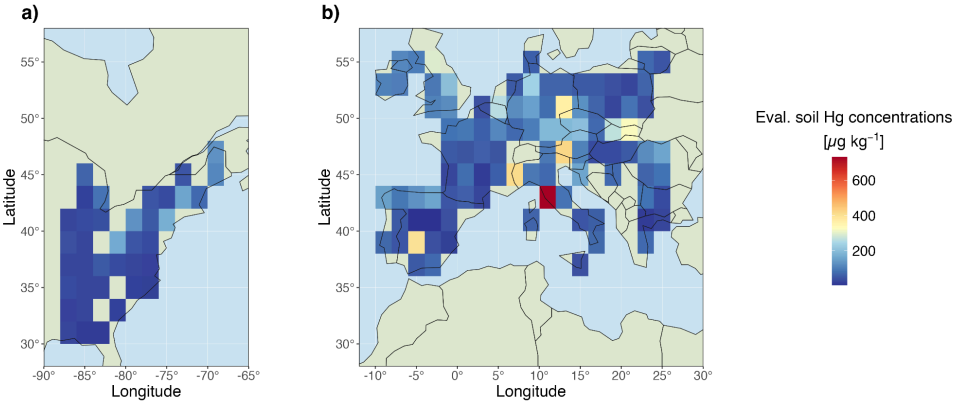
977



978

979 **Figure A3**: Kinetic of pools equilibrium during the spin-up period illustrating the stability of
980 the different pools after 24,360 years of simulations. Vertical dashed lines represent runs of
981 the C and Hg soil modules in insolation for 3000 years.

982



983

984 **Figure A4**: Evaluation concentrations Hg data a) 0 -5 cm soil depth in the U.S. area, b) 0 -20
985 cm depth in the E.U. area

986

https://doi.org/10.5194/egusphere-2026-5859
Preprint. Discussion started: 4 November 2026
© Author(s) 2026. CC BY 4.0 License.

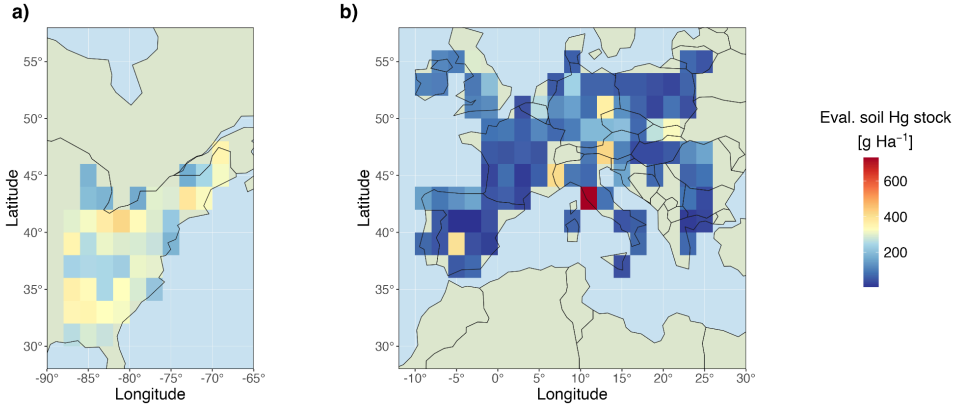


Figure A5: Evaluation Hg soils stocks a) 0-100 cm soil depth in the U.S. area, b) 0-20 cm depth in the E.U. area

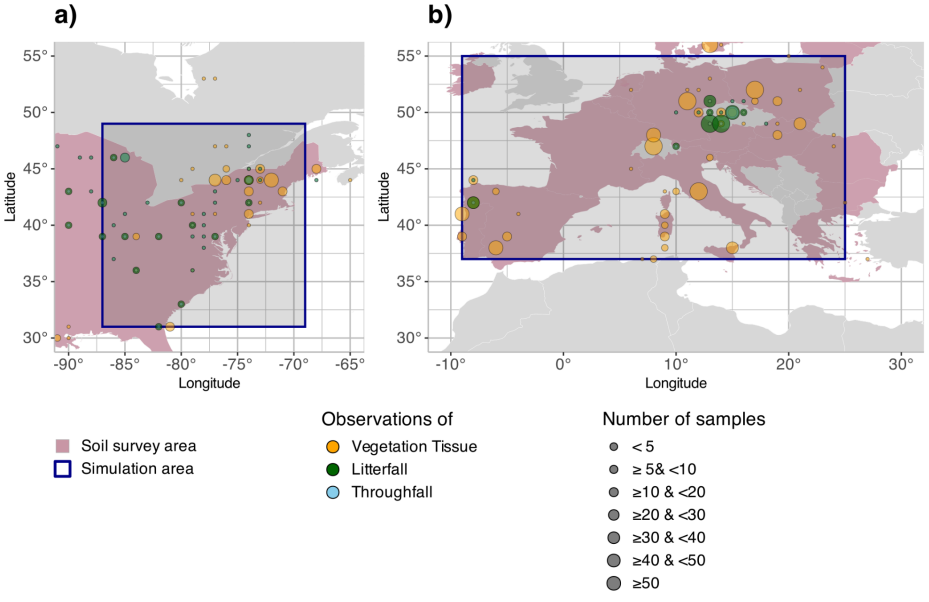
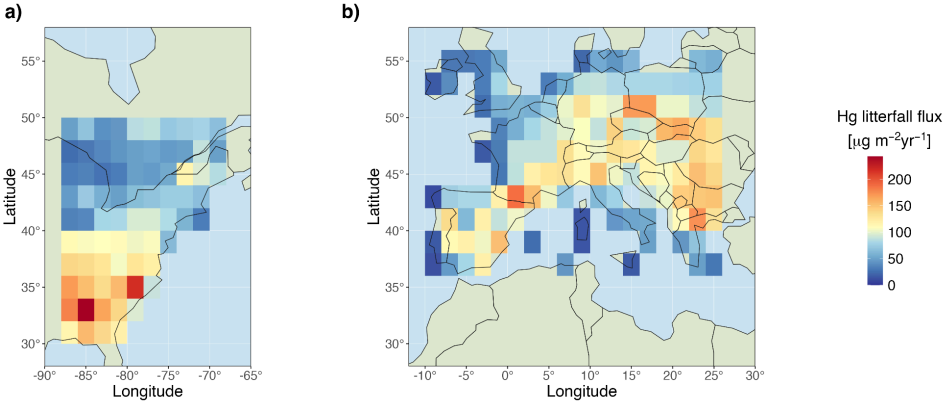


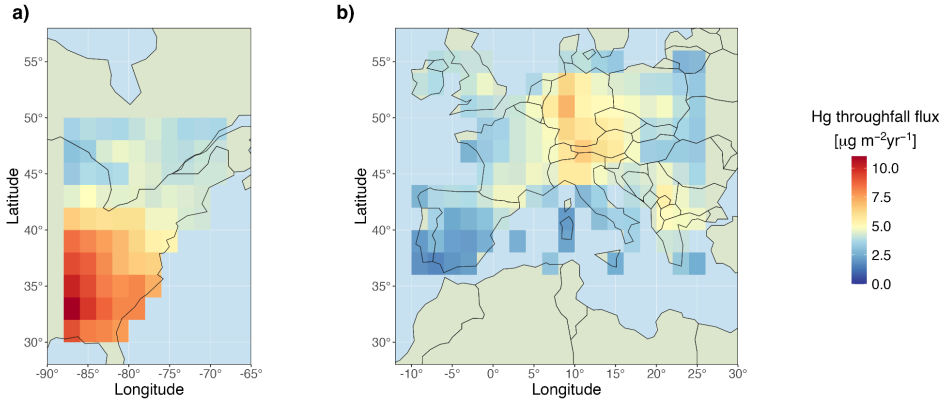
Figure A6: Map of available vegetation (Zhou and Obrist, 2021), litterfall, throughfall evaluation data from (Sereni et al., 2026) (symbolic points) and soil surveys with associated digital mapping evaluation data (colored area) (Ballabio et al., 2021; Olson et al., 2022)

https://doi.org/10.5194/egusphere-2026-5859
Preprint. Discussion started: 4 November 2026
© Author(s) 2026. CC BY 4.0 License.

996 zoomed over the two simulation area represented with the square(68-88°W, 30-50°N) and
997 -10-26°E, 35-55°N.
998
999



1000
1001 **Figure A7**: Mean annual Hg litterfall flux per m^{-2}, calculated as a PFT-weighted average
1002 based on the PFT coverage within each grid cell.
1003



1005
1006 **Figure A8:** Mean annual Hg throughfall flux per m^{-2}, calculated as a PFT-weighted average
1007 based on the PFT coverage within each grid cell.
1008

https://doi.org/10.5194/egusphere-2026-5859
Preprint. Discussion started: 4 November 2026
© Author(s) 2026. CC BY 4.0 License.

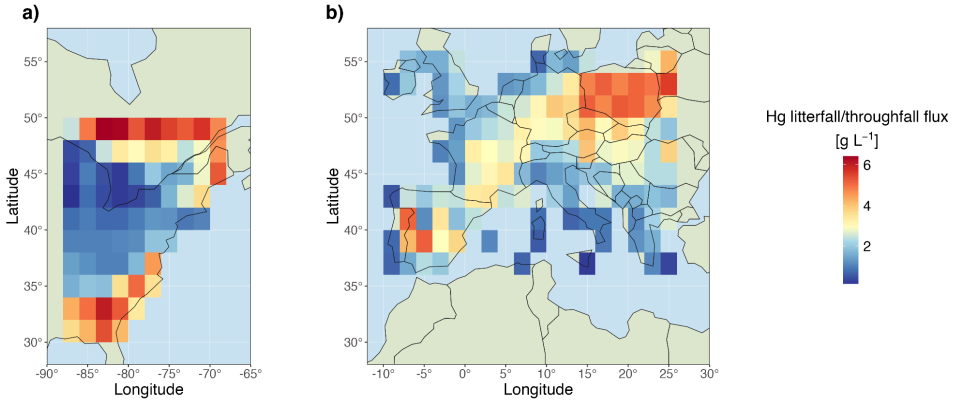


Figure A9: Mean annual Hg LF/TF per m^{-2} calculated as a PFT-weighted average based on the PFT coverage within each grid cell.

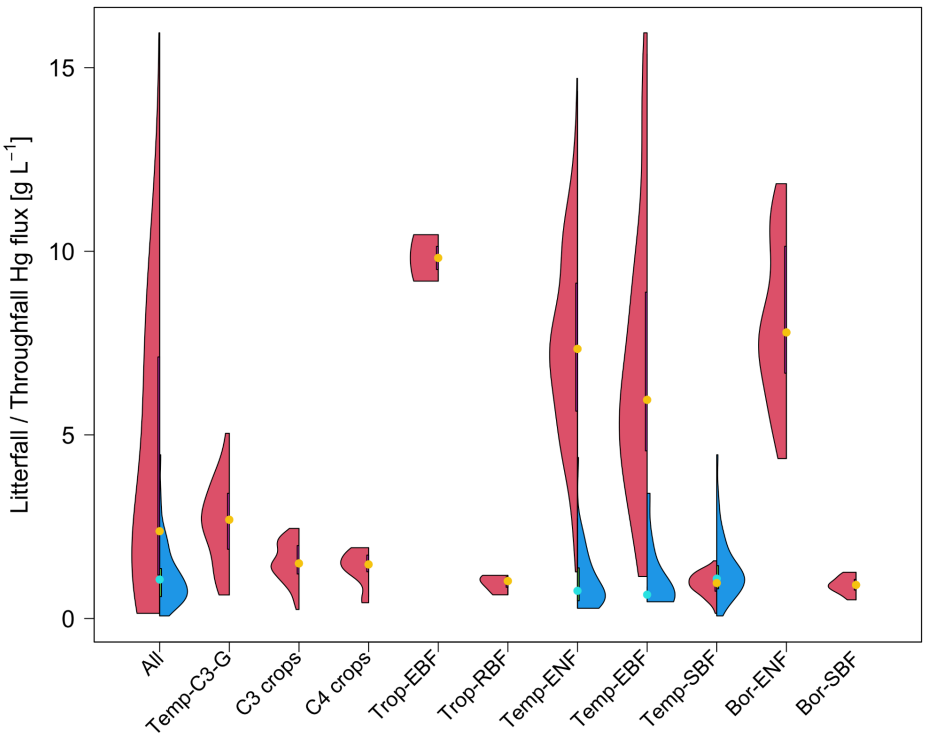


Figure A10: Litterfall/Throughfall Hg ratio [g L^{-1}] for the different PFTs represented in the simulation area (red) compared to litterfall/throughfall flux from evaluation data (Sereni et al., 2026) (blue). The number of samples is indicated Table A3. Temp-C3-G: temperate C3

https://doi.org/10.5194/egusphere-2026-5859
Preprint. Discussion started: 4 November 2026
© Author(s) 2026. CC BY 4.0 License.

grass; C3 crops: C3 crops; C4 crops: C4 crops; Trop-EBF: Tropical evergreen broadleaf forest; Trop-RBF: Tropical raingreen broadleaf forest; Temp-ENF: Temperate evergreen needleleaf forest; Temp-EBF: Temperate evergreen broadleaf forest; Temp-SBF: Temperate summergreen broadleaf forest; Bor-ENF: Boreal evergreen needleleaf forest; Bor-SBF: Boreal summergreen broadleaf forest.

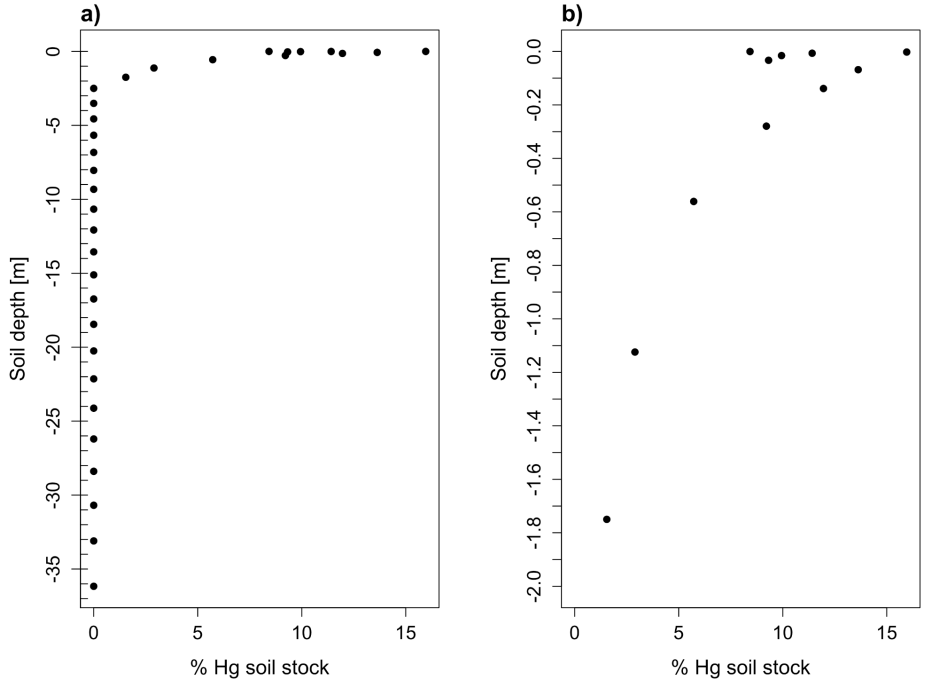


Figure A11: Vertical distribution of modeled Hg soil stocks (expressed as a percentage of the total column stock). Points are centered on each soil layer. a) Entire soil column, b) Top 2 m.

https://doi.org/10.5194/egusphere-2026-5859
Preprint. Discussion started: 4 November 2026
© Author(s) 2026. CC BY 4.0 License.

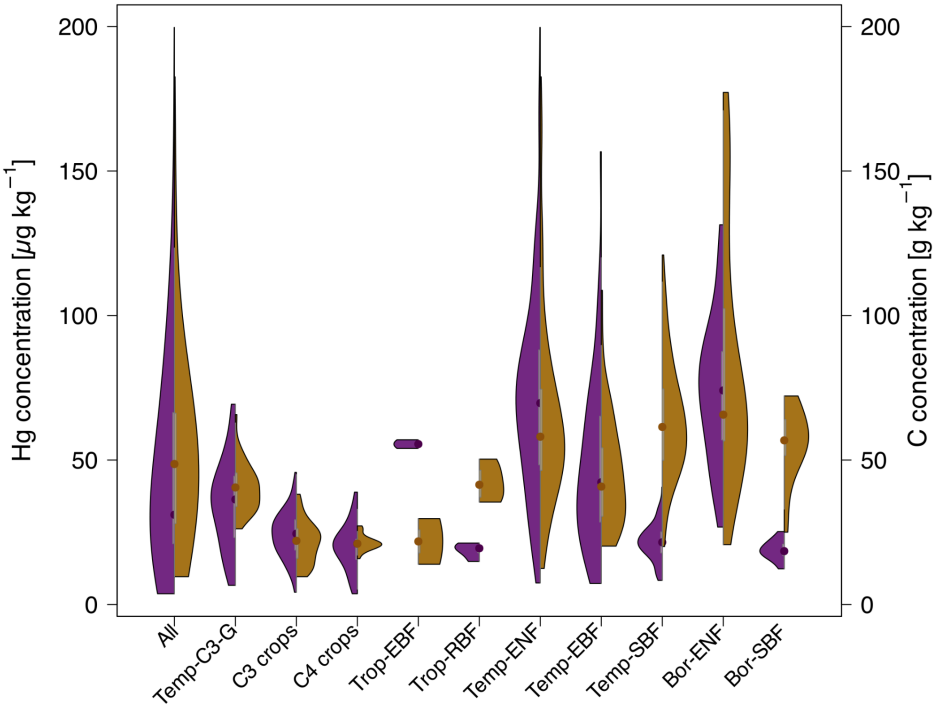


Figure A12: Soil Hg [µg kg^{-1}] in purple and C [g kg^{-1}] in brown concentrations over the 0-20 m soil column for the different plant functional types. Temp-C3-G: temperate C3 grass; C3 crops: C3 crops; C4 crops: C4 crops; Trop-EBF: Tropical evergreen broadleaf forest; Trop-RBF: Tropical raingreen broadleaf forest; Temp-ENF: Temperate evergreen needleleaf forest; Temp-EBF: Temperate evergreen broadleaf forest; Temp-SBF: Temperate summergreen broadleaf forest; Bor-ENF: Boreal evergreen needleleaf forest; Bor-SBF: Boreal summergreen broadleaf forest.

https://doi.org/10.5194/egusphere-2026-5859
Preprint. Discussion started: 4 November 2026
© Author(s) 2026. CC BY 4.0 License.

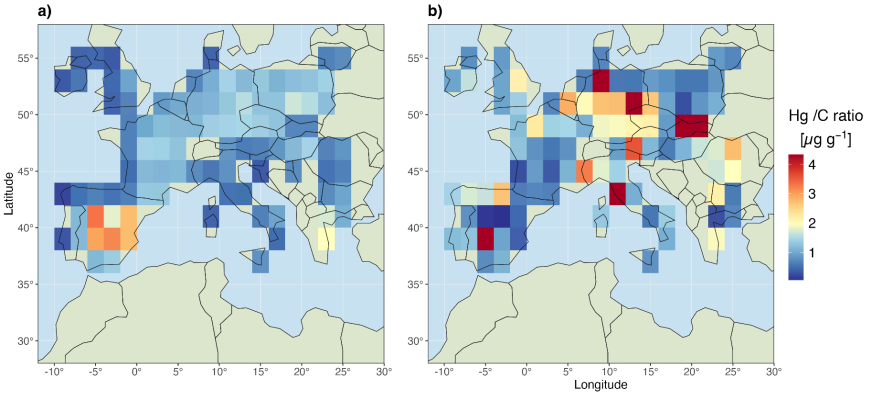


Figure A13: Hg/C ratio in µg g^{-1}, a) from model output, b) from JRC evaluation data.

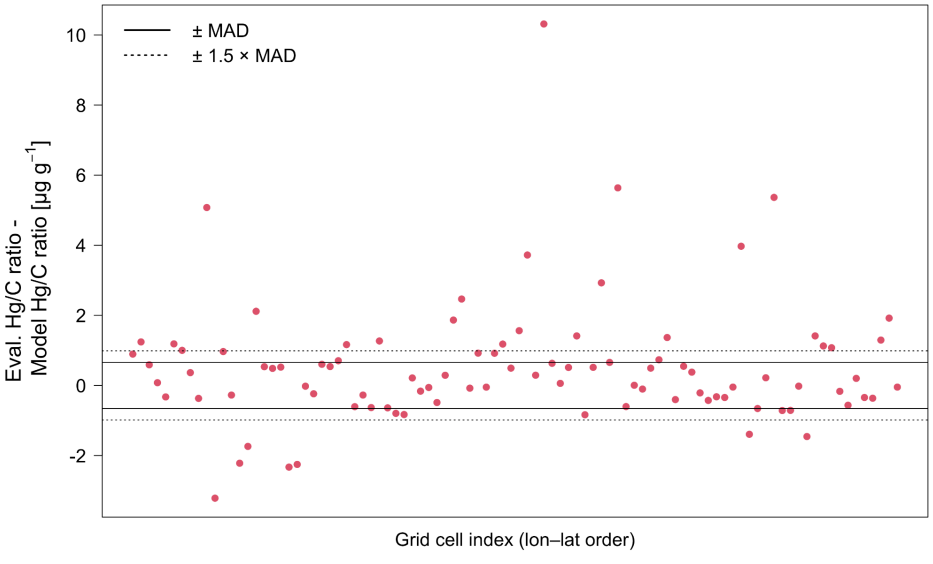


Figure A14: Residuals of Hg/C ratios for the E.U simulation area. ± MAD of evaluation data and ± 1.5 MAD of evaluation data are represented to scale residuals.

https://doi.org/10.5194/egusphere-2026-5859
Preprint. Discussion started: 4 November 2026
© Author(s) 2026. CC BY 4.0 License.

7. Code availability

The ORCHIDEE-Hg v1.0 source code is publicly available through the ORCHIDEE-Hg/code repository and is archived on Zenodo (https://doi.org/10.5281/zenodo.22811755, Sereni and Angot, 2026b). The repository contains the ORCHIDEE-Hg v1.0 code, including the Hg module stored at Orchidee_files/travail/ORCHIDEE-Hg_v1_0/ORCHIDEE/src_stomate/stomate_Hg.f90. The code used to generate the figures and perform the model evaluation is available through the ORCHIDEE-Hg/figure_code repository, also archived on Zenodo (https://doi.org/10.5281/zenodo.22814362, Sereni and Angot, 2026c).

8. Data availability

The datasets associated with this study are publicly available through Zenodo (single entry point: (https://doi.org/10.5281/zenodo.22811840, Sereni and Angot, 2026a). The ORCHIDEE-Hg/input_data repository contains the input datasets required for the simulations, including atmospheric Hg deposition fields generated with GEOS-Chem. Model outputs from the simulations over Eastern US, Western Europe, and Eastern Europe are provided in the ORCHIDEE-Hg/output_data repository.

https://doi.org/10.5194/egusphere-2026-5859
Preprint. Discussion started: 4 November 2026
© Author(s) 2026. CC BY 4.0 License.

Author contribution

LS led the model development with contributions from ES. EJ reviewed the code. ES, SPK, DL, RL, HZ developed significant previous versions of the ORCHIDEE model. HA conceived the study and supervised LS and EJ. LS wrote the manuscript with contributions and revisions from all authors. We thank Clémence Foucher for designing Figure 1.

Competing interests

HA serves as topic editor for the special issue to which this paper belongs.

Ackowledgments

We gratefully acknowledge LSCE (Laboratoires des Sciences du Climat et de l'Environnement, Gif-sur-Yvette, France) for providing access to the Obelix computing cluster used for the ORCHIDEE-Hg simulations. LS also acknowledges ENS-PSL for hosting support through an institutional hosting agreement, which provided a valuable environment for the development of this work. GEOS-Chem simulations used in this paper were performed using the GRICAD infrastructure (https://gricad.univ-grenoble-alpes.fr) , which is supported by Grenoble research communities.

Financial support

This research was supported by the ANR ATOX project (ANR-24-CE01-7616) and the SNSF PRIMA ACCLIMATE project (grant no. PR00P2_208610).

https://doi.org/10.5194/egusphere-2026-5859
Preprint. Discussion started: 4 November 2026
© Author(s) 2026. CC BY 4.0 License.

References

AMAP: AMAP Assessment 2021: Mercury in the Arctic | AMAP, Arctic Monitoring and Assessment Programme, 2021, viii, Tromso, https://www.amap.no/documents/doc/amap-assessment-2021-mercury-in-the-arctic/3581 (last access: 2 September 2024), 2021.

Amos, H. M., Jacob, D. J., Streets, D. G., and Sunderland, E. M.: Legacy impacts of all-time anthropogenic emissions on the global mercury cycle, Glob. Biogeochem. Cycles, 27, 410–421, https://doi.org/10.1002/gbc.20040, 2013.

Amos, H. M., Sonke, J. E., Obrist, D., Robins, N., Hagan, N., Horowitz, H. M., Mason, R. P., Witt, M., Hedgecock, I. M., Corbitt, E. S., and Sunderland, E. M.: Observational and Modeling Constraints on Global Anthropogenic Enrichment of Mercury, Environ. Sci. Technol., 49, 4036–4047, https://doi.org/10.1021/es5058665, 2015.

Ballabio, C., Jiskra, M., Osterwalder, S., Borrelli, P., Montanarella, L., and Panagos, P.: A spatial assessment of mercury content in the European Union topsoil, Sci. Total Environ., 769, 144755, https://doi.org/10.1016/j.scitotenv.2020.144755, 2021.

Blackwell, B. D., Driscoll, C. T., Maxwell, J. A., and Holsen, T. M.: Changing climate alters inputs and pathways of mercury deposition to forested ecosystems, Biogeochemistry, 119, 215–228, https://doi.org/10.1007/s10533-014-9961-6, 2014.

Bowring, S. P. K., Lauerwald, R., Guenet, B., Zhu, D., Guimberteau, M., Tootchi, A., Ducharne, A., and Ciais, P.: ORCHIDEE MICT-LEAK (r5459), a global model for the production, transport, and transformation of dissolved organic carbon from Arctic permafrost regions – Part 1: Rationale, model description, and simulation protocol, Geosci. Model Dev., 12, 3503–3521, https://doi.org/https://doi.org/10.5194/gmd-12-3503-2019, 2019.

Bowring, S. P. K., Lauerwald, R., Guenet, B., Zhu, D., Guimberteau, M., Regnier, P., Tootchi, A., Ducharne, A., and Ciais, P.: ORCHIDEE MICT-LEAK (r5459), a global model for the production, transport, and transformation of dissolved organic carbon from Arctic permafrost regions – Part 2: Model evaluation over the Lena River basin, Geosci. Model Dev., 13, 507–520, https://doi.org/https://doi.org/10.5194/gmd-13-507-2020, 2020.

Bring, A., Fedorova, I., Dibike, Y., Hinzman, L., Mård, J., Mernild, S. H., Prowse, T., Semenova, O., Stuefer, S. L., and Woo, M.-K.: Arctic terrestrial hydrology: A synthesis of processes, regional effects, and research challenges, J. Geophys. Res. Biogeosciences, 121, 621–649, https://doi.org/10.1002/2015JG003131, 2016.

de Brogniez, D., Ballabio, C., Stevens, A., Jones, R. J. A., Montanarella, L., and van Wesemael, B.: A map of the topsoil organic carbon content of Europe generated by a generalized additive model, Eur. J. Soil Sci., https://doi.org/10.1111/ejss.12193, 2015.

Camino-Serrano, M., Guenet, B., Luyssaert, S., Ciais, P., Bastrikov, V., De Vos, B., Gielen, B., Gleixner, G., Jornet-Puig, A., Kaiser, K., Kothawala, D., Lauerwald, R., Peñuelas, J., Schrumpf, M., Vicca, S., Vuichard, N., Walmsley, D., and Janssens, I. A.: ORCHIDEE-SOM: modeling soil

https://doi.org/10.5194/egusphere-2026-5859
Preprint. Discussion started: 4 November 2026
© Author(s) 2026. CC BY 4.0 License.

organic carbon (SOC) and dissolved organic carbon (DOC) dynamics along vertical soil profiles in Europe, Geosci. Model Dev., 11, 937–957, https://doi.org/10.5194/gmd-11-937-2018, 2018.

Chambers, J. M. (Ed.): Graphical methods for data analysis, Repr., Chapman & Hall, New York, 395 pp., 1998.

Chen, B., Lu, Q., Wei, L., Fu, W., Wei, Z., and Tian, S.: Global predictions of topsoil organic carbon stocks under changing climate in the 21st century, Sci. Total Environ., 908, 168448, https://doi.org/10.1016/j.scitotenv.2023.168448, 2024a.

Chen, L., Zhou, J., Guo, L., Bian, X., Xu, Z., Chen, Q., Wen, S.-H., Wang, K., and Liu, Y.-R.: Global Distribution of Mercury in Foliage Predicted by Machine Learning, Environ. Sci. Technol., 58, 15629–15637, https://doi.org/10.1021/acs.est.4c00636, 2024b.

Dastoor, A., Angot, H., Bieser, J., Brocza, F., Edwards, B., Feinberg, A., Feng, X., Geyman, B., Gournia, C., He, Y., Hedgecock, I. M., Ilyin, I., Kirk, J., Lin, C.-J., Lehnherr, I., Mason, R., McLagan, D., Muntean, M., Rafaj, P., Roy, E. M., Ryjkov, A., Selin, N. E., De Simone, F., Soerensen, A. L., Steenhuisen, F., Travnikov, O., Wang, S., Wang, X., Wilson, S., Wu, R., Wu, Q., Zhang, Y., Zhou, J., Zhu, W., and Zolkos, S.: The Multi-Compartment Hg Modeling and Analysis Project (MCHgMAP): mercury modeling to support international environmental policy, Geosci. Model Dev., 18, 2747–2860, https://doi.org/10.5194/gmd-18-2747-2025, 2025.

Driscoll, C. T., Mason, R. P., Chan, H. M., Jacob, D. J., and Pirrone, N.: Mercury as a Global Pollutant: Sources, Pathways, and Effects, , https://doi.org/10.1021/es305071v, 2013.

Druel, A., Peylin, P., Krinner, G., Ciais, P., Viovy, N., Peregon, A., Bastrikov, V., Kosykh, N., and Mironycheva-Tokareva, N.: Towards a more detailed representation of high-latitude vegetation in the global land surface model ORCHIDEE (ORC-HL-VEGv1.0), Geosci. Model Dev., 10, 4693–4722, https://doi.org/10.5194/gmd-10-4693-2017, 2017.

Fabre, C., Sonke, J. E., Tananaev, N., and Teisserenc, R.: Organic carbon and mercury exports from pan-Arctic rivers in a thawing permafrost context – A review, Sci. Total Environ., 954, 176713, https://doi.org/10.1016/j.scitotenv.2024.176713, 2024.

Feinberg, A., Jiskra, M., Borrelli, P., Biswakarma, J., and Selin, N. E.: Deforestation as an Anthropogenic Driver of Mercury Pollution, Environ. Sci. Technol., 58, 3246–3257, https://doi.org/10.1021/acs.est.3c07851, 2024.

Feinberg, A., Sonke, J. E., Cuevas, C. A., Li, M.-L., Acuña, A. U., Fernandez, R. P., Plane, J. M. C., Villamayor, J., and Saiz-Lopez, A.: Shifts in Atmospheric Composition Since the Preindustrial Era Modified the Transport and Deposition of Mercury, AGU Adv., 7, e2025AV002158, https://doi.org/10.1029/2025AV002158, 2026.

Friedli, H. R., Radke, L. F., Payne, N. J., McRae, D. J., Lynham, T. J., and Blake, T. W.: Mercury in vegetation and organic soil at an upland boreal forest site in Prince Albert National Park, Saskatchewan, Canada, J. Geophys. Res. Biogeosciences, 112, https://doi.org/10.1029/2005JG000061, 2007.

https://doi.org/10.5194/egusphere-2026-5859
Preprint. Discussion started: 4 November 2026
© Author(s) 2026. CC BY 4.0 License.

Fu, X., Zhang, H., Liu, C., Zhang, H., Lin, C.-J., and Feng, X.: Significant Seasonal Variations in Isotopic Composition of Atmospheric Total Gaseous Mercury at Forest Sites in China Caused by Vegetation and Mercury Sources, Environ. Sci. Technol., 53, 13748–13756, https://doi.org/10.1021/acs.est.9b05016, 2019.

Gao, X., Yuan, W., Chen, J., Huang, F., Wang, Z., Gong, Y., Zhang, Y., Liu, Y., Zhang, T., and Zheng, W.: Tracing the source and transport of Hg during pedogenesis in strongly weathered tropical soil using Hg isotopes, Geochim. Cosmochim. Acta, 361, 101–112, https://doi.org/10.1016/j.gca.2023.10.009, 2023.

Grigal, D. F.: Inputs and outputs of mercury from terrestrial watersheds: a review, Environ. Rev., 10, 1–39, https://doi.org/10.1139/a01-013, 2002.

Grimaldi, C., Grimaldi, M., and Guedron, S.: Mercury distribution in tropical soil profiles related to origin of mercury and soil processes, Sci. Total Environ., 401, 121–129, https://doi.org/10.1016/j.scitotenv.2008.04.001, 2008.

Gruba, P., Socha, J., Pietrzykowski, M., and Pasichnyk, D.: Tree species affects the concentration of total mercury (Hg) in forest soils: Evidence from a forest soil inventory in Poland, Sci. Total Environ., 647, 141–148, https://doi.org/10.1016/j.scitotenv.2018.07.452, 2019.

Guimberteau, M., Zhu, D., Maignan, F., Huang, Y., Yue, C., Dantec-Nédélec, S., Ottlé, C., Jornet-Puig, A., Bastos, A., Laurent, P., Goll, D., Bowring, S., Chang, J., Guenet, B., Tifafi, M., Peng, S., Krinner, G., Ducharne, A., Wang, F., Wang, T., Wang, X., Wang, Y., Yin, Z., Lauerwald, R., Joetzjer, E., Qiu, C., Kim, H., and Ciais, P.: ORCHIDEE-MICT (v8.4.1), a land surface model for the high latitudes: model description and validation, Geosci. Model Dev., 11, 121–163, https://doi.org/10.5194/gmd-11-121-2018, 2018.

Guo, W., Liu, M., Zhang, Q., Deng, Y., Chu, Z., Qin, H., Li, Y., Liu, Y.-R., Zhang, H., Zhang, W., Tao, S., and Wang, X.: Warming-Induced Vegetation Greening May Aggravate Soil Mercury Levels Worldwide, Environ. Sci. Technol., 58, 15078–15089, https://doi.org/10.1021/acs.est.4c01923, 2024.

Hararuk, O., Obrist, D., and Luo, Y.: Modelling the sensitivity of soil mercury storage to climate-induced changes in soil carbon pools, Biogeosciences, 10, 2393–2407, https://doi.org/10.5194/bg-10-2393-2013, 2013.

Huber, P. J.: Robust statistics, Wiley, New York, NY, 1981.

Jia, L., Huang, J.-H., Wang, X., Yuan, W., Pu, Q., Zhang, H., Liu, N., Zhou, J., Zhu, X., Sun, M., Driscoll, C. T., Wang, F., Lin, C.-J., and Feng, X.: Climate and plant traits drive a cross-continental imbalance in atmospheric Hg uptake, Nat. Commun., 17, 5504, https://doi.org/10.1038/s41467-026-74746-x, 2026.

Jiskra, M., Wiederhold, J. G., Skyllberg, U., Kronberg, R.-M., Hajdas, I., and Kretzschmar, R.: Mercury Deposition and Re-emission Pathways in Boreal Forest Soils Investigated with Hg Isotope Signatures, Environ. Sci. Technol., 49, 7188–7196, https://doi.org/10.1021/acs.est.5b00742, 2015.

https://doi.org/10.5194/egusphere-2026-5859
Preprint. Discussion started: 4 November 2026
© Author(s) 2026. CC BY 4.0 License.

Jiskra, M., Sonke, J. E., Obrist, D., Bieser, J., Ebinghaus, R., Myhre, C. L., Pfaffhuber, K. A., Wängberg, I., Kyllönen, K., Worthy, D., Martin, L. G., Labuschagne, C., Mkololo, T., Ramonet, M., Magand, O., and Dommergue, A.: A vegetation control on seasonal variations in global atmospheric mercury concentrations, Nat. Geosci., 11, 244–250, https://doi.org/10.1038/s41561-018-0078-8, 2018.

Jobbágy, E. G. and Jackson, R. B.: The Vertical Distribution of Soil Organic Carbon and Its Relation to Climate and Vegetation, Ecol. Appl., 10, 423–436, https://doi.org/10.1890/1051-0761(2000)010%5B0423:TVDOSO%5D2.0.CO;2, 2000.

Koven, C., Friedlingstein, P., Ciais, P., Khvorostyanov, D., Krinner, G., and Tarnocai, C.: On the formation of high-latitude soil carbon stocks: Effects of cryoturbation and insulation by organic matter in a land surface model, Geophys. Res. Lett., 36, https://doi.org/10.1029/2009GL040150, 2009.

Koven, C. D., Riley, W. J., and Stern, A.: Analysis of Permafrost Thermal Dynamics and Response to Climate Change in the CMIP5 Earth System Models, J. Clim., 26, 1877–1900, https://doi.org/10.1175/JCLI-D-12-00228.1, 2013.

Koven, C. D., Schuur, E. A. G., Schädel, C., Bohn, T. J., Burke, E. J., Chen, G., Chen, X., Ciais, P., Grosse, G., Harden, J. W., Hayes, D. J., Hugelius, G., Jafarov, E. E., Krinner, G., Kuhry, P., Lawrence, D. M., MacDougall, A. H., Marchenko, S. S., McGuire, A. D., Natali, S. M., Nicolsky, D. J., Olefeldt, D., Peng, S., Romanovsky, V. E., Schaefer, K. M., Strauss, J., Treat, C. C., and Turetsky, M.: A simplified, data-constrained approach to estimate the permafrost carbon–climate feedback, Philos. Trans. R. Soc. Math. Phys. Eng. Sci., 373, 20140423, https://doi.org/10.1098/rsta.2014.0423, 2015.

Krinner, G., Viovy, N., de Noblet-Ducoudré, N., Ogée, J., Polcher, J., Friedlingstein, P., Ciais, P., Sitch, S., and Prentice, I. C.: A dynamic global vegetation model for studies of the coupled atmosphere-biosphere system, Glob. Biogeochem. Cycles, 19, https://doi.org/10.1029/2003GB002199, 2005.

Laacouri, A., Nater, E. A., and Kolka, R. K.: Distribution and Uptake Dynamics of Mercury in Leaves of Common Deciduous Tree Species in Minnesota, U.S.A., Environ. Sci. Technol., 47, 10462–10470, https://doi.org/10.1021/es401357z, 2013.

Lauerwald, R., Regnier, P., Camino-Serrano, M., Guenet, B., Guimberteau, M., Ducharne, A., Polcher, J., and Ciais, P.: ORCHILEAK (revision 3875): a new model branch to simulate carbon transfers along the terrestrial–aquatic continuum of the Amazon basin, Geosci. Model Dev., 10, 3821–3859, https://doi.org/10.5194/gmd-10-3821-2017, 2017.

Leys, C., Ley, C., Klein, O., Bernard, P., and Licata, L.: Detecting outliers : Do not use standard deviation around the mean , use absolute deviation around the median, J. Exp. Soc. Psychol., 49, 764–766, https://doi.org/10.1016/j.jesp.2013.03.013, 2013.

Lim, A. G., Jiskra, M., Sonke, J. E., Loiko, S. V., Kosykh, N., and Pokrovsky, O. S.: A revised pan-Arctic permafrost soil Hg pool based on Western Siberian peat Hg and carbon observations, Biogeosciences, 17, 3083–3097, https://doi.org/https://doi.org/10.5194/bg-17-3083-2020, 2020.

https://doi.org/10.5194/egusphere-2026-5859
Preprint. Discussion started: 4 November 2026
© Author(s) 2026. CC BY 4.0 License.

Liu, Y.-R., Guo, L., Yang, Z., Xu, Z., Zhao, J., Wen, S.-H., Delgado-Baquerizo, M., and Chen, L.: Multidimensional Drivers of Mercury Distribution in Global Surface Soils: Insights from a Global Standardized Field Survey, Environ. Sci. Technol., 57, 12442–12452, https://doi.org/10.1021/acs.est.3c04313, 2023.

Ma, H., Cheng, H., Guo, F., Zhang, L., Tang, S., Yang, Z., and Peng, M.: Distribution of mercury in foliage, litter and soil profiles in forests of the Qinling Mountains, China, Environ. Res., 211, 113017, https://doi.org/10.1016/j.envres.2022.113017, 2022.

Mann, H. B. and Whitney, D. R.: On a Test of Whether one of Two Random Variables is Stochastically Larger than the Other, Ann. Math. Stat., 18, 50–60, https://doi.org/10.1214/aoms/1177730491, 1947.

Matthews, E.: Global litter production, pools, and turnover times: Estimates from measurement data and regression models, J. Geophys. Res. Atmos., 102, 18771–18800, https://doi.org/10.1029/97JD02956, 1997.

Mcgill, R., Tukey, J. W., and Larsen, W. A.: Variations of Box Plots, Am. Stat., 32, 12–16, https://doi.org/10.1080/00031305.1978.10479236, 1978.

Muntean, M., Janssens-Maenhout, G., Song, S., Giang, A., Selin, N. E., Zhong, H., Zhao, Y., Olivier, J. G. J., Guizzardi, D., Crippa, M., Schaaf, E., and Dentener, F.: Evaluating EDGARv4.tox2 speciated mercury emissions ex-post scenarios and their impacts on modelled global and regional wet deposition patterns, Atmos. Environ., 184, 56–68, https://doi.org/10.1016/j.atmosenv.2018.04.017, 2018.

Obrist, D., Johnson, D. W., Lindberg, S. E., Luo, Y., Hararuk, O., Bracho, R., Battles, J. J., Dail, D. B., Edmonds, R. L., Monson, R. K., Ollinger, S. V., Pallardy, S. G., Pregitzer, K. S., and Todd, D. E.: Mercury Distribution Across 14 U.S. Forests. Part I: Spatial Patterns of Concentrations in Biomass, Litter, and Soils, Environ. Sci. Technol., 45, 3974–3981, https://doi.org/10.1021/es104384m, 2011.

Obrist, D., Kirk, J. L., Zhang, L., Sunderland, E. M., Jiskra, M., and Selin, N. E.: A review of global environmental mercury processes in response to human and natural perturbations: Changes of emissions, climate, and land use, Ambio, 47, 116–140, https://doi.org/10.1007/s13280-017-1004-9, 2018.

Olson, C. I., Geyman, B. M., Thackray, C. P., Krabbenhoft, D. P., Tate, M. T., Sunderland, E. M., and Driscoll, C. T.: Mercury in soils of the conterminous United States: patterns and pools, Environ. Res. Lett., 17, 074030, https://doi.org/10.1088/1748-9326/ac79c2, 2022.

Orgiazzi, A., Ballabio, C., Panagos, P., Jones, A., and Fernández-Ugalde, O.: LUCAS Soil, the largest expandable soil dataset for Europe: a review, Eur. J. Soil Sci., 69, 140–153, https://doi.org/10.1111/ejss.12499, 2018.

Panagos, P., Jiskra, M., Borrelli, P., Liakos, L., and Ballabio, C.: Mercury in European topsoils: Anthropogenic sources, stocks and fluxes, Environ. Res., 201, 111556, https://doi.org/10.1016/j.envres.2021.111556, 2021.

https://doi.org/10.5194/egusphere-2026-5859
Preprint. Discussion started: 4 November 2026
© Author(s) 2026. CC BY 4.0 License.



Qiu, C., Zhu, D., Ciais, P., Guenet, B., Peng, S., Krinner, G., Tootchi, A., Ducharne, A., and Hastie, A.: Modelling northern peatland area and carbon dynamics since the Holocene with the ORCHIDEE-PEAT land surface model (SVN r5488), Geosci. Model Dev., 12, 2961–2982, https://doi.org/10.5194/gmd-12-2961-2019, 2019.

Qiu, C., Ciais, P., Bian, C., Liu, L., Guenet, B., Zhu, D., Chen, X., Fang, C., Xia, J., Peregon, A. M., Kosykh, N. P., Mironycheva-Tokareva, N. P., Dušek, J., López-Blanco, E., Xiao, J., Li, X., Desai, A. R., Euskirchen, E., Edgar, C., Ratcliffe, J., Peichl, M., Noumonvi, K. D., Fortuniak, K., Pawlak, W., Lohila, A., Korkiakoski, M., Aurela, M., and Kalhori, A.: Modeling Sub-Grid Peatland Vegetation Dynamics in the ORCHIDEE-PEAT Land Surface Model, J. Adv. Model. Earth Syst., 18, e2025MS005257, https://doi.org/10.1029/2025MS005257, 2026.

R Core Team: R: A Language and Environment for Statistical Computing, R Foundation for Statistical Computing, Vienna, Austria, 2024.

Rea, A. W., Lindberg, S. E., Scherbatskoy, T., and Keeler, G. J.: Mercury Accumulation in Foliage over Time in Two Northern Mixed-Hardwood Forests, Water. Air. Soil Pollut., 133, 49–67, https://doi.org/10.1023/A:1012919731598, 2002.

Reimann, C., Fabian, K., Birke, M., Filzmoser, P., Demetriades, A., Négrel, P., Oorts, K., Matschullat, J., de Caritat, P., Albanese, S., Anderson, M., Baritz, R., Batista, M. J., Bel-lan, A., Cicchella, D., De Vivo, B., De Vos, W., Dinelli, E., Ďuriš, M., Dusza-Dobek, A., Eggen, O. A., Eklund, M., Ernsten, V., Flight, D. M. A., Forrester, S., Fügedi, U., Gilucis, A., Gosar, M., Gregorauskiene, V., De Groot, W., Gulan, A., Halamić, J., Haslinger, E., Hayoz, P., Hoogewerff, J., Hrvatovic, H., Husnjak, S., Jähne-Klingberg, F., Janik, L., Jordan, G., Kaminari, M., Kirby, J., Klos, V., Kwećko, P., Kuti, L., Ladenberger, A., Lima, A., Locutura, J., Lucivjansky, P., Mann, A., Mackovych, D., McLaughlin, M., Malyuk, B. I., Maquil, R., Meuli, R. G., Mol, G., O'Connor, P., Ottesen, R. T., Pasnieczna, A., Petersell, V., Pfleiderer, S., Poňavič, M., Prazeres, C., Radusinović, S., Rauch, U., Salpeteur, I., Scanlon, R., Schedl, A., Scheib, A., Schoeters, I., Šefčik, P., Sellersjö, E., Slaninka, I., Soriano-Disla, J. M., Šorša, A., Svrkota, R., Stafilov, T., Tarvainen, T., Tendavilov, V., Valera, P., Verougstraete, V., Vidojević, D., Zissimos, A., Zomeni, Z., and Sadeghi, M.: GEMAS: Establishing geochemical background and threshold for 53 chemical elements in European agricultural soil, Appl. Geochem., 88, 302–318, https://doi.org/10.1016/j.apgeochem.2017.01.021, 2018.

Richardson, J. B. and Friedland, A. J.: Mercury in coniferous and deciduous upland forests in northern New England, USA: implications of climate change, Biogeosciences, 12, 6737–6749, https://doi.org/10.5194/bg-12-6737-2015, 2015.

Richardson, J. B., Friedland, A. J., Engerbretson, T. R., Kaste, J. M., and Jackson, B. P.: Spatial and vertical distribution of mercury in upland forest soils across the northeastern United States, Environ. Pollut., 182, 127–134, https://doi.org/10.1016/j.envpol.2013.07.011, 2013.

Schaefer, K., Elshorbany, Y., Jafarov, E., Schuster, P. F., Striegl, R. G., Wickland, K. P., and Sunderland, E. M.: Potential impacts of mercury released from thawing permafrost, Nat. Commun., 11, 1–6, https://doi.org/10.1038/s41467-020-18398-5, 2020.

Schulzweida, U.: CDO User Guide, , https://doi.org/10.5281/zenodo.2558193, 2019.

https://doi.org/10.5194/egusphere-2026-5859
Preprint. Discussion started: 4 November 2026
© Author(s) 2026. CC BY 4.0 License.

Schuster, P. F., Schaefer, K. M., Aiken, G. R., Antweiler, R. C., Dewild, J. F., Gryziec, J. D., Gusmeroli, A., Hugelius, G., Jafarov, E., Krabbenhoft, D. P., Liu, L., Herman-Mercer, N., Mu, C., Roth, D. A., Schaefer, T., Striegl, R. G., Wickland, K. P., and Zhang, T.: Permafrost Stores a Globally Significant Amount of Mercury, Geophys. Res. Lett., 45, 2017GL075571, https://doi.org/10.1002/2017GL075571, 2018.

Schuur, E. A. G. and Mack, M. C.: Ecological Response to Permafrost Thaw and Consequences for Local and Global Ecosystem Services, Annu. Rev. Ecol. Evol. Syst., 49, 279–301, https://doi.org/10.1146/annurev-ecolsys-121415-032349, 2018.

Selin, N. E.: Global Biogeochemical Cycling of Mercury: A Review | Annual Reviews, Vol. 34, 43–63, https://doi.org/https://doi.org/10.1146/annurev.environ.051308.084314, 2009.

Selin, N. E., Jacob, D. J., Yantosca, R. M., Strode, S., Jaeglé, L., and Sunderland, E. M.: Global 3-D land-ocean-atmosphere model for mercury: Present-day versus preindustrial cycles and anthropogenic enrichment factors for deposition, Glob. Biogeochem. Cycles, 22, https://doi.org/10.1029/2007GB003040, 2008.

Sereni, L. and Angot, H.: ORCHIDEE-Hg, https://doi.org/10.5281/zenodo.22811841, 2026a.

Sereni, L. and Angot, H.: ORCHIDEE-Hg/code, https://doi.org/10.5281/zenodo.22811756, 2026b.

Sereni, L. and Angot, H.: ORCHIDEE-Hg/figure_code, https://doi.org/10.5281/zenodo.22814363, 2026c.

Sereni, L., Jahangir, E., Feng, X., Fernandez, I. J., Fostier, A.-H., Grigal, D., Gómez-Armesto, A., Kolka, R., Munthe, J., Navrátil, T., Nóvoa-Muñoz, J. C., Parente-Sendín, A., Pontevedra-Pombal, X., Silva-Filho, E. V., and Angot, H.: Standardizing mercury litterfall and throughfall data for comparative research: Introducing the MFallDa global database, Data Brief, 68, 113206, https://doi.org/10.1016/j.dib.2026.113206, 2026.

Shah, V., Jacob, D. J., Thackray, C. P., Wang, X., Sunderland, E. M., Dibble, T. S., Saiz-Lopez, A., Černušák, I., Kellö, V., Castro, P. J., Wu, R., and Wang, C.: Improved Mechanistic Model of the Atmospheric Redox Chemistry of Mercury, Environ. Sci. Technol., 55, 14445–14456, https://doi.org/10.1021/acs.est.1c03160, 2021.

Sitch, S., O'Sullivan, M., Robertson, E., Friedlingstein, P., Albergel, C., Anthoni, P., Arneth, A., Arora, V. K., Bastos, A., Bastrikov, V., Bellouin, N., Canadell, J. G., Chini, L., Ciais, P., Falk, S., Harris, I., Hurtt, G., Ito, A., Jain, A. K., Jones, M. W., Joos, F., Kato, E., Kennedy, D., Klein Goldewijk, K., Kluzek, E., Knauer, J., Lawrence, P. J., Lombardozzi, D., Melton, J. R., Nabel, J. E. M. S., Pan, N., Peylin, P., Pongratz, J., Poulter, B., Rosan, T. M., Sun, Q., Tian, H., Walker, A. P., Weber, U., Yuan, W., Yue, X., and Zaehle, S.: Trends and Drivers of Terrestrial Sources and Sinks of Carbon Dioxide: An Overview of the TRENDY Project, Glob. Biogeochem. Cycles, 38, e2024GB008102, https://doi.org/10.1029/2024GB008102, 2024.

Skyllberg, U., Xia, K., Bloom, P. R., Nater, E. A., and Bleam, W. F.: Binding of Mercury(II) to Reduced Sulfur in Soil Organic Matter along Upland-Peat Soil Transects, J. Environ. Qual., 29, 855–865, https://doi.org/10.2134/jeq2000.00472425002900030022x, 2000.

https://doi.org/10.5194/egusphere-2026-5859
Preprint. Discussion started: 4 November 2026
© Author(s) 2026. CC BY 4.0 License.

Smith, D. B., Cannon, W. F., Woodruff, L. G., Garrett, R. G., Klassen, R., Kilburn, J. E., Horton, J. D., King, H. D., Goldhaber, M. B., and Morrison, J. M.: Major- and trace-element concentrations in soils from two continental-scale transects of the United States and Canada, Open-File Report, 2005–1253, U.S. Geological Survey, https://doi.org/10.3133/ofr20051253, 2005.

Smith-Downey, N. V., Sunderland, E. M., and Jacob, D. J.: Anthropogenic impacts on global storage and emissions of mercury from terrestrial soils: Insights from a new global model, J. Geophys. Res. Biogeosciences, 115, https://doi.org/10.1029/2009JG001124, 2010.

Sommar, J., Osterwalder, S., and Zhu, W.: Recent advances in understanding and measurement of Hg in the environment: Surface-atmosphere exchange of gaseous elemental mercury (Hg0), Sci. Total Environ., 2020.

Song, S., Selin, N. E., Gratz, L. E., Ambrose, J. L., Jaffe, D. A., Shah, V., Jaeglé, L., Giang, A., Yuan, B., Kaser, L., Apel, E. C., Hornbrook, R. S., Blake, N. J., Weinheimer, A. J., Mauldin III, R. L., Cantrell, C. A., Castro, M. S., Conley, G., Holsen, T. M., Luke, W. T., and Talbot, R.: Constraints from observations and modeling on atmosphere–surface exchange of mercury in eastern North America, Elem. Sci. Anthr., 4, 000100, https://doi.org/10.12952/journal.elementa.000100, 2016.

Sonke, J. E., Angot, H., Zhang, Y., Poulain, A., Björn, E., and Schartup, A.: Global change effects on biogeochemical mercury cycling, Ambio, 52, 853–876, https://doi.org/10.1007/s13280-023-01855-y, 2023.

Travnikov, O., Angot, H., Artaxo, P., Bencardino, M., Bieser, J., D'Amore, F., Dastoor, A., De Simone, F., Diéguez, M. del C., Dommergue, A., Ebinghaus, R., Feng, X. B., Gencarelli, C. N., Hedgecock, I. M., Magand, O., Martin, L., Matthias, V., Mashyanov, N., Pirrone, N., Ramachandran, R., Read, K. A., Ryjkov, A., Selin, N. E., Sena, F., Song, S., Sprovieri, F., Wip, D., Wängberg, I., and Yang, X.: Multi-model study of mercury dispersion in the atmosphere: atmospheric processes and model evaluation, Atmos. Chem. Phys., 17, 5271–5295, https://doi.org/10.5194/acp-17-5271-2017, 2017.

University of East Anglia Climatic Research Unit, Harris, I., Osborn, T. J., Jones, P., and Lister, D.: CRU JRA v2.4: A forcings dataset of gridded land surface blend of Climatic Research Unit (CRU) and Japanese reanalysis (JRA) data; Jan.1901 - Dec.2022 (2.4), https://doi.org/10.1038/s41597-020-0453-3, 2023.

Wang, X., Yuan, W., Lin, C.-J., Zhang, L., Zhang, H., and Feng, X.: Climate and Vegetation As Primary Drivers for Global Mercury Storage in Surface Soil, Env. Sci Technol, https://doi.org/10.1021/acs.est.9b02386, 2019.

Willmott, C. J. and Matsuura, K.: Advantages of the mean absolute error (MAE) over the root mean square error (RMSE) in assessing average model performance, Clim. Res., 30, 79–82, https://doi.org/10.3354/cr030079, 2005.

Yuan, T., Zhang, P., Song, Z., Huang, S., Wang, X., and Zhang, Y.: Buffering effect of global vegetation on the air-land exchange of mercury: Insights from a novel terrestrial mercury

https://doi.org/10.5194/egusphere-2026-5859
Preprint. Discussion started: 4 November 2026
© Author(s) 2026. CC BY 4.0 License.



model based on CESM2-CLM5, Environ. Int., 174, 107904, https://doi.org/10.1016/j.envint.2023.107904, 2023.

Yue, C., Ciais, P., Luyssaert, S., Cadule, P., Harden, J., Randerson, J., Bellassen, V., Wang, T., Piao, S. L., Poulter, B., and Viovy, N.: Simulating boreal forest carbon dynamics after stand-replacing fire disturbance: insights from a global process-based vegetation model, Biogeosciences, 10, 8233–8252, https://doi.org/10.5194/bg-10-8233-2013, 2013.

Yue, C., Ciais, P., Cadule, P., Thonicke, K., and van Leeuwen, T. T.: Modelling the role of fires in the terrestrial carbon balance by incorporating SPITFIRE into the global vegetation model ORCHIDEE – Part 2: Carbon emissions and the role of fires in the global carbon balance, Geosci. Model Dev., 8, 1321–1338, https://doi.org/10.5194/gmd-8-1321-2015, 2015.

Yue, C., Ciais, P., Luyssaert, S., Li, W., McGrath, M. J., Chang, J., and Peng, S.: Representing anthropogenic gross land use change, wood harvest, and forest age dynamics in a global vegetation model ORCHIDEE-MICT v8.4.2, Geosci. Model Dev., 11, 409–428, https://doi.org/10.5194/gmd-11-409-2018, 2018.

Zhang, H., Holmes, C. D., and Wu, S.: Impacts of changes in climate, land use and land cover on atmospheric mercury, Atmos. Environ., 141, 230–244, https://doi.org/10.1016/j.atmosenv.2016.06.056, 2016.

Zhang, H., Lauerwald, R., Regnier, P., Ciais, P., Van Oost, K., Naipal, V., Guenet, B., and Yuan, W.: Estimating the lateral transfer of organic carbon through the European river network using a land surface model, Earth Syst. Dyn., 13, 1119–1144, https://doi.org/10.5194/esd-13-1119-2022, 2022.

Zhao, Z., Ciais, P., Guenet, B., Stegehuis, A., Lauerwald, R., Regnier, P., Yuan, C., Lin, G., Luo, Y., Zhu, X., Li, R., Gou, R., Wu, J., and Li, W.: ORCHIDEE-MAN: Incorporating Mangrove Processes in the Global Vegetation Model of ORCHIDEE, J. Adv. Model. Earth Syst., 17, e2025MS005185, https://doi.org/10.1029/2025MS005185, 2025.

Zhou, J. and Obrist, D.: Global Mercury Assimilation by Vegetation, Environ. Sci. Technol., https://doi.org/10.1021/acs.est.1c03530, 2021.

Zhou, J., Obrist, D., Dastoor, A., Jiskra, M., and Ryjkov, A.: Vegetation uptake of mercury and impacts on global cycling, Nat. Rev. Earth Environ., 1–16, https://doi.org/10.1038/s43017-021-00146-y, 2021.

Zhu, W., Lin, C.-J., Wang, X., Sommar, J., Fu, X., and Feng, X.: Global observations and modeling of atmosphere–surface exchange of elemental mercury: a critical review, Atmos. Chem. Phys., 16, 4451–4480, https://doi.org/10.5194/acp-16-4451-2016, 2016.

Harmonized World Soil Database version 2.0, FAO; International Institute for Applied Systems Analysis (IIASA);, https://doi.org/10.4060/cc3823en, 2023.